DIGITALCOMMONS
@WAYNESTATE

Wayne State University

Wayne State University Theses

1-1-2017

Seismic Anisotropy As A Function Of Mineralogy And Rock Type In Chester Gneiss Dome, Southeast Vermont

Brittany Watling
Wayne State University,

Follow this and additional works at: https://digitalcommons.wayne.edu/oa_theses

 Part of the Geology Commons

Recommended Citation
Watling, Brittany, "Seismic Anisotropy As A Function Of Mineralogy And Rock Type In Chester Gneiss Dome, Southeast Vermont" (2017). *Wayne State University Theses.* 593.
https://digitalcommons.wayne.edu/oa_theses/593

This Open Access Thesis is brought to you for free and open access by DigitalCommons@WayneState. It has been accepted for inclusion in Wayne State University Theses by an authorized administrator of DigitalCommons@WayneState.

SEISMIC ANISOTROPY AS A FUNCTION OF MINERALOGY AND ROCK TYPE IN CHESTER GNEISS DOME, SOUTHEAST VERMONT

by

BRITTANY WATLING

THESIS

Submitted to the Graduate School

of Wayne State University,

Detroit, Michigan

in partial fulfillment of the requirements

for the degree of

MASTER OF SCIENCE

2017

MAJOR: GEOLOGY

Approved By:

5-5-2017

Advisor Date

© COPYRIGHT BY

BRITTANY WATLING

2017

All Rights Reserved

ACKNOWLEDGEMENTS

A special thank you to Sarah Brownlee for allowing me to do research for her NSF project.

I would like to thank my friends and family for the support and keeping me sane.

TABLE OF CONTENTS

LIST OF TABLES

LIST OF FIGURES

Chapter 1: Introduction

Most of our knowledge of the structure of the deep Earth comes from seismic observations. For example, the inference that the outer core is liquid stems from the observation that shear waves do not travel through the outer core. Seismic observations have also contributed to our understanding of the composition of the deep Earth. As an example, the location of the boundary between the crust and the mantle is marked by a significant seismic discontinuity known as the Mohorovicic discontinuity, which results from a strong contrast in seismic properties between the felsic crust and the mafic mantle (Halchuk and Mereu, 1990). Even within the crust, variations in seismic properties, mainly seismic velocity—the speed at which seismic waves travel through a material—have informed our understanding of the layered structure of the upper crust. In the lower crust, the situation is more complicated.

Our understanding of the composition of the lower crust is derived mainly from a combination of 1) surface heat flow measurements, which are lower than would be expected if the rock types found near the surface made up the entire crust, and 2) observations of faster seismic velocities in the lower crust. The combination of low surface heat flow and high seismic velocities in the deep crust has led to the inference that the lower crust must be more mafic than the upper crust (Rudnick and Fountain, 1995; Klemperer, 1987). Yet difficulties arise when trying to confirm specific rock types in the lower crust because there are many candidate rocks that have similar seismic velocities, and we cannot directly sample rocks from deeper than ~13 km (currently, the deepest drill hole reaches a depth of 12.3 km; Pavlenkova, 1992). Thus, there is a need to go beyond simple seismic velocities in order to better constrain the composition and structure of the lower crust.

Seismic anisotropy is the directional dependence of seismic velocity. Most seismic studies of anisotropy have focused on anisotropy in the mantle, mainly because the mantle constitutes most of the material seismic waves travel through, and thus most of the signal is coming from the mantle. In fact, the crust is often ignored completely because compared to the signal from the mantle, even anisotropic crust is not expected to contribute much to the overall signal of anisotropy simply because the crust is so thin relative to the mantle. Mantle anisotropy is also relatively simple, and generally understood as being derived from the preferred crystallographic orientation of olivine (Anderson, 1989; Christen and Crosson, 1968). Seismic anisotropy in the crust, on the other hand, is significantly more complicated.

Seismic anisotropy in the crust has 3 main causes: 1) layering (e.g. Backus, 1965), 2) oriented cracks and fractures (Siegesmund et al., 1991), and 3) crystallographic preferred orientation of minerals (Siegesmund and Kruhl, 1991).The first two causes, layering and oriented cracks, are most important in the upper crust, where sedimentary layering is a dominant structural feature, and where pressure is low enough that oriented cracks are open and able to influence seismic waves. In this study, we are focused on the lower crust, where pressures are high enough to close cracks, and layering is expected to be at a smaller length-scale than seismic wavelengths due to the metamorphic nature of the rocks, e.g. gneissic banding. The dominant cause of anisotropy in the lower crust is thus expected to be the preferred orientation of minerals in the rocks.

Crystallographic preferred orientation, or CPO, occurs during deformation at pressure and temperature conditions that favor crystal-plastic deformation over brittle deformation. Development of mineral CPO produces seismic anisotropy because individual mineral crystals have highly anisotropic elastic properties. For example, seismic waves traveling parallel to the c-

axis of biotite travel at almost half the speed (4.0 km/s) of those traveling perpendicular to the c-axis, or within the basal plane (7.8 km/s). The elastic tensor of a rock is the aggregate of all of the individual minerals in their respective orientations. The result is that a rock that has developed mineral CPOs in response to deformation will have an anisotropic elastic tensor that is a function of not only the particular minerals are present in the rock, but also how the rock has been deformed. This means that if we understand how the elastic tensor is controlled by the mineralogy and deformation of specific rocks, we can do the inverse, and use seismic determinations of the large-scale elastic tensor to infer rock type and mineralogy, as well as the deformation processes that are active.

In this study, we will focus on characterizing the elastic tensor of rocks from the Chester gneiss dome in southeastern Vermont in order to contribute to the database of crustal rock elastic tensors, and improve our ability to use seismically determined elastic tensors to constrain rock type, mineralogy, and deformation processes in the middle and lower crust. We will investigate the dependence of seismic anisotropy on mineralogy and rock type for four rock groups based on compositional and textural variations: mafic gneiss, felsic gneiss, mafic schist, and felsic schist. Our hypotheses are focused on the effects of the particular minerals within these rocks.

1.1 Hypotheses

We have developed three general hypotheses based on previously published work (Brownlee et al., 2011). We focus on four basic mineral groups: quartz, feldspar, mica, and amphibole, and we expect each mineral group to have different effects on the components of the aggregate rock elastic tensor.

1.1.1 Hypothesis 1

Quartz and feldspar are expected to decrease the magnitude of seismic anisotropy. We expect our felsic rocks, especially the felsic gneiss group, will have lower magnitude of anisotropy resulting from higher quartz and feldspar content. For rocks rich in quartz, we also expect the symmetry of the aggregate elastic tensor to have a higher orthorhombic component because quartz CPOs usually result in alignment of the fast axis of quartz within the fast plane of mica. For rocks rich in feldspar, we expect low anisotropy and very low-order symmetry because feldspar does not develop strong CPOs, and has triclinic symmetry in its elastic tensor.

1.1.2 Hypothesis 2

Mica is expected to increase the magnitude of seismic anisotropy and the hexagonal symmetry component. Micas have the highest single crystal anisotropy of any mineral, and develop very strong preferred orientations, so we expect rocks rich in mica to have the highest anisotropy. Thus we expect the schists to have higher anisotropy than the gneisses. Mica also has nearly hexagonal symmetry in its elastic properties (monoclinic crystal structure with pseudo-hexagonal symmetry), so we expect elastic tensors from rocks with significant mica (~>10% by volume), to have a large hexagonal symmetry component.

1.1.3 Hypothesis 3

Amphibole is expected to increase anisotropy and increase the orthorhombic symmetry component. Amphibole, hornblende in our samples, has single crystal anisotropy of 24.1 % (this is the difference between the fastest and slowest velocity as a percentage of the median velocity), which is slightly lower in magnitude than quartz (24.3 %) or feldspar (29.3 %), but amphibole generally develops much stronger preferred orientations than either quartz or feldspar, so we expect rocks rich in amphibole to have higher anisotropy. The symmetry of amphibole elastic

properties is actually triclinic, but amphibole CPOs usually result in nearly orthorhombic symmetry with a fast, a slow, and an intermediate velocity direction. Rocks rich in amphibole, such as mafic gneisses and schists will thus have higher anisotropies than their felsic counterparts, and a higher orthorhombic symmetry component.

1.2 Geologic Background

The Appalachian Mountains started to shape over 480 million years ago. This mountain range formed during three orogenic events stretching from the Ordovician to the Permian: the Taconic, Acadian and Alleghanian (Hatcher, 2010). During the Acadian there were two main periods of deformation in eastern Vermont, a nappe stage and a dome stage, described by Rosenfeld (1968). This study focuses on Chester dome, which lies in the northern Appalachians of southeastern Vermont. It is a north-south elongated mantled gneiss dome with a variety of origin models that depend on the stage of orogenesis in which the dome might have developed. These models include diapiric rise (Teyssier and Whitney, 2002), nappe development (Thompson, 1950; Rosenfeld, 1968; Thompson et al., 1968), and extensional unroofing (Teyssier and Whitney, 2002; Lee et al., 2004).

Chester Dome contains many varieties of metamorphic rocks expected to be found in the deeper parts of the crust, making it an ideal location for studies of the seismic properties of lower crustal rocks. Early studies (Thompson, 1950; Rosenfeld, 1968) have shown that in most locations in the dome the foliation is parallel to the bedding and is attributed to nappe development prior to dome development. Our samples were collected from several locations on the dome edges, and within the dome. In this study, we focus on two sampling locations (Figure 1), one on the southwest margin and the other on the southeast margin of the dome.

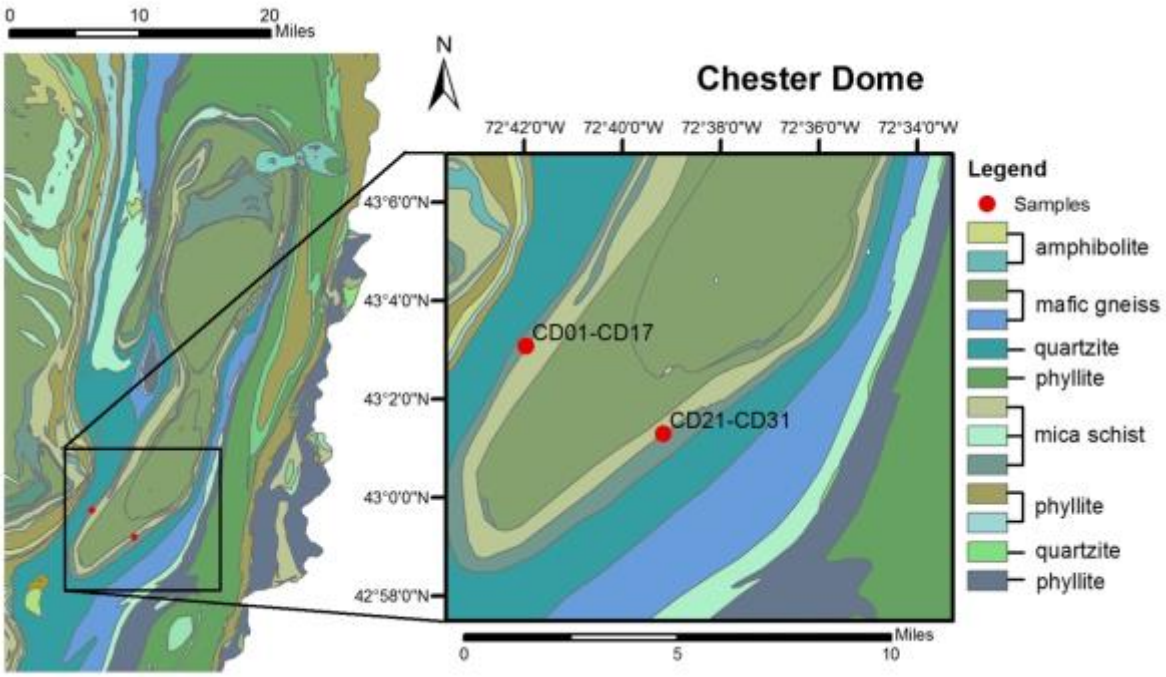

Figure 1. Generalized geological map of southeastern Vermont. Chester dome characterized by the dark green peanut shape. Samples from this study were located in the southern half of Chester dome.

1.2.1 Southwestern Margin

The samples from the southwestern margin were taken from the Townshend Dam spillway. This outcrop described by Karabinos (2002) includes at least three geologic formations: Hoosac, Pinney Hollow, and Moretown. These formations range in age from the Neoproterozoic to lower Cambrian. The Hoosac Formation is the oldest formation and is composed of plagioclase schist and gneiss. The Pinney Hollow Formation contains mainly pelitic schist and amphibolite. The Moretown Formation encompasses many layers of mafic and pelitic schist.

1.2.2 Southeastern Margin

The samples collected from the southeast margin of the dome were taken along Ellen Ware Road just outside of Townshend, Vermont. The units found in this area range in age from the early

Mesoproterozoic to the lower Ordivician. The formations listed from the oldest to youngest are the Mount Holly Complex, Hoosac Formation and Moretown Formation. The Mount Holly Complex is composed of felsic schist and gneiss. The Hoosac and Moretown formations in this location are similar to those in the spillway. In this location, the Hoosac Formation contains mainly plagioclase schist, and the Moretown Formation contains mafic and pelitic schists.

Chapter 2: Materials and Methods

We collected 21 oriented samples from two areas in the southern part of Chester dome, near Townshend, VT. The samples are grouped into four groups based on rock type: felsic schist, mafic schist, felsic gneiss, and mafic gneiss.

2.1 Thin Section Preparation

We prepared thin sections from each sample using standard methods. First, we cut a billet approximately 2x2x4 cm, such that the longest dimension is parallel to the lineation in the sample, and one of the shorter dimensions is perpendicular to the foliation. Ultimately, a thin section is made from the surface that is perpendicular to the foliation and parallel to the lineation. The surface is sanded in stages using silicon carbide sandpaper in grits of 240, 400, 600 and 800, and then attached to a 2.5x4.6 cm glass slide using epoxy resin. When the epoxy is cured, the billet is cut about 0.5mm from the slide to create a thin section. Each thin section was sanded in stages with the silicon carbide sandpaper in grits of 400, 600, 800 and 1200 until the rock was approximately 30 μm thick. We used quartz and feldspar birefringence to determine thickness. After grinding down to the desired thickness, the thin sections were polished using diamond polish at 3, 1, and 0.1 μm grit sizes using a Leco Spectrum System 1000 grinder/polisher. Diamond polish was followed by polishing for ~3 hrs in a colloidal silica solution for electron backscatter diffraction.

2.2 Petrography and Point Counting

We made basic petrographic observations of each thin section using a Nikon Eclipse 50i petrographic microscope, and we determined modal mineral proportions for each sample using a Pelcon automatic point counting stage.

2.3 Electron Backscatter Diffraction (EBSD)

Electron backscatter diffraction (EBSD) was used to measure the crystallographic orientation of minerals in the samples. The EBSD process starts by accelerating a beam of electrons towards the sample surface, which is oriented at ~20˚ to the electron beam. The electrons are diffracted as they interact with the surface of the crystal lattice creating a diffraction pattern that can be captured by a phosphor screen on the EBSD camera. The diffraction pattern consists of bands, called Kikuchi bands that are related to planes of atoms in the crystal structure. The specific pattern observed is related to both the mineral phase, and its orientation. EBSD software digitizes the patterns detected by the phosphor screen, and identifies individual bands and their orientation, and automatically compares the measured pattern to predicted patterns for a given list of possible minerals, and calculates a pattern misfit, which is the mean angular deviation (MAD) between the measured and predicted patterns, for all possible predicted patterns (each mineral in the list in all possible orientations). The pattern with the lowest MAD is chosen as the indexed mineral phase and orientation. We collected phase and orientation data in square grid maps, using 100 µm step sizes. The maps were collected in beam-scan mode, where the electron beam moves to each point in a ~1x1 mm area, and then the stage moves and another map is collected, until the entire thin section is mapped. The individual maps are then stitched together into one map of the thin section.

The EBSD measurements were completed at University of California, Santa Barbara using a FEI Quanta 400f scanning electron microscope (SEM) with a field emission gun, an Oxford Instruments EBSD camera and HKL Channel 5 software. The thin sections were coated with roughly 5-6 nm of carbon to prevent charging of the surface in the SEM chamber. The sample surface was tilted at 70º from horizontal (20º from the incoming beam). We used an accelerating voltage of 20 kV, a spot size of 6.0, and the step size of each map was 100 microns.

In addition to mineral phase and orientation data, at each point in the map energy dispersive X-ray spectrographic (EDS) data was also obtained. The EDS data was collected for eight elements: Na, Mg, Al, SI, K, Ca, Ti, and Fe. This data was used to identify any points that were assigned the wrong phase when processing the EBSD data. Mis-indexing occurs when the predicted EBSD pattern for the wrong mineral phase has the lowest MAD with the measured pattern. This can occur for many reasons, and it is most common in geologic samples where there are many different mineral phases, some of which have similar crystal structures. Sample preparation can also have an effect on the quality of automatic indexing due to the detail, or lack thereof, in the diffraction pattern as a result of the preparation quality. Collecting simultaneous chemical data is the best way to ensure the correct mineral phase has been chosen. To eliminate mis-indexed points we used an algorithm written by Sarah Brownlee that compares the measured elemental composition to the expected composition of the minerals in the sample by calculating a root-mean-squared (RMS) difference between the two. The lowest RMS indicates the mineral phase that best matches the chemical data. Data points for which the EBSD indexed mineral did not match the best fit to the chemical data were deleted.

2.4 Crystallographic Preferred Orientations

We calculated orientation distribution functions (ODF) from the EBSD data for the main mineral phases in each sample using the MTEX toolbox (Mainprice et al., 2015). The ODF is a measure of the crystallographic preferred orientations (CPOs). We used one point-per-grain data for the ODF calculations to avoid skewing the distribution by including multiples of the same orientation from single grains. The ODFs are visualized using contoured pole figures of particular crystallographic directions. The pole figures were produced using the MTEX toolbox(Mainprice et al., 2015).

The texture index, or ODF-J is a measure of the strength of a CPO, and is a comparison of the measured ODF to a random ODF of the same mineral. An ODF-J of 1 occurs when the measured ODF is the same as a random distribution, and suggests a weak CPO. Pole figure J-values are similar comparisons between the measured distribution of one particular crystallographic direction, and a random distribution.

2.5 Elastic Tensor and Seismic Anisotropy Calculations

Elastic tensors for each sample were calculated from the EBSD data, modal mineral proportions, and single crystal elastic constants (Cij) for each mineral present in each rock. The calculation involves first rotating the single crystal Cij into the correct orientation given by the EBSD data at each point in the data set. The tensors are then averaged together, first for each mineral phase to produce a single mineral aggregate tensor, and then the single mineral aggregate tensors are averaged together using weights according to their modal proportion in the sample. We used a Voigt-Reus-Hill averaging scheme, which is an average of the constant stress (Voigt) and constant strain (Reuss) averaging methods. Tables report uncertainty bounds given by the Voight and Reuss end-member average tensors.

Seismic velocity stereonets were produced to visualize the anisotropy of seismic wave velocities through the elastic tensor of the given rock. The stereonets are produced using the Christoffel equation can then be used to calculate the seismic velocity in all possible wave propagation directions. The Vp anisotropy, AVp, is the difference between the maximum and minimum Vp divided by the median Vp and is expressed as a percentage:

$$AVp = \frac{Vp_{max} - Vp_{min}}{(Vp_{max} + Vp_{min}/2)} * 100$$

The shear wave anisotropy, AVs, depends on propagation direction. AVs is the difference between Vs1 and Vs2 in the same propagation direction, (i), divided by the median Vs1 for all propagation directions, also expressed as a percentage:

$$AVs = \frac{Vs1(i) - Vs2(i)}{(Vs1_{max} + Vs1_{min}/2)} * 100$$

The maximum AVs occurs in the direction in which the fast shear wave is much faster than the orthogonally polarized slow shear wave. AVs max usually occurs for wave propagation parallel to the foliation. The time delay between the two shear waves, DVs, is equivalent to seismic observations of shear wave splitting, and is calculated as seconds of delay per km of wave propagation:

$$DVs(i) = \frac{1}{Vs2(i)} - \frac{1}{Vs1(i)}$$

where i is the propagation direction, and Vs1 and Vs2 are the shear wave velocities in that direction given in km/s, resulting in a delay time in seconds of delay per kilometer of material.

2.6 Symmetry decomposition

The elastic tensors for each sample were also decomposed into six symmetry components using the vector projection method described in Browaeys and Chevrot (2004) as implemented in a Matlab script written by Sarah Brownlee. The method involves projecting a vectorized version of the full elastic tensor onto vectors corresponding to different orthogonal symmetry elements. The six symmetry components that we used are: isotropic, hexagonal, orthorhombic, tetragonal, monoclinic, and triclinic. The symmetry components are removed in order of decreasing order of symmetry. First, the isotropic component is removed, followed by hexagonal, tetragonal, orthorhombic, and monoclinic, in that order. The remaining tensor is assigned to triclinic symmetry. This method does ignore some possible symmetry components, such as trigonal. By

decomposing the elastic tensors, we can relate the elastic symmetry components to the rock type and mineralogy of each sample.

Chapter 3: Results

3.1 Composition

The felsic gneiss group has the highest modal content of feldspar ranging 13.5-53.5% by volume (Table 3.1). The mafic gneiss group has the highest hornblende content ranging 30.6-70.9%, and overall this group has the lowest amount of modal quartz. Both felsic groups have the highest modal quartz content ranging 25.1-54.6%. On average the mafic schist has the highest modal biotite content and chlorite content ranging 15.1-49.1% and 2.2-13.6%, respectively. The felsic schist group has the highest modal mica, with muscovite accounting for 22.3-43.9%. The felsic schist contains more garnet than the mafic schist. Both mafic groups have more hornblende and chlorite than the felsic groups.

Table 1. Mineral compositions for each sample

	Modal Proportions (%)							
	Quartz	Feldspar	Biotite	Muscovite	Chlorite	Hornblende	Garnet	Pyrite
Felsic Gneiss								
CD06	30.4	44.6	4.0	9.4	4.0		6.9	
CD07	31.6	41.2	2.8	8.5	3.7	12.2		
CD15	35.6	22.4	8.4	23.9	4.9		4.8	
CD19	23.2	53.5	10.8	12.6				
CD21	25.1	38.1	7.3	29.5				
CD22	42.8	35.2	17.5	4.5				
CD27	54.6	13.5	12.2	13.9	4.3		1.5	
Mafic Gneiss								
CD03	10.6	14.3	4.2			70.9		
CD10	8.3	15.2	10.6	13.5		52.4		
CD13	26.4	13.8	0.6		10.7	48.5		
CD24	32.5	19.7	7.9	9.2		30.7		
Felsic Schist								
CD01	32.3	21.7	18.1	22.3			5.7	
CD09	31.3	10.3	16.6	37.8			4.0	
CD14	33.8	14.5	14.9	35.7			1.2	
CD17	25.1	25.6	0.5	30.6	10.1		8.1	
CD31	5.6	24.9	14.4	43.9	6.5		4.8	
Mafic Schist								
CD02	21.7	18.1	15.1	9.4	13.6	16.3	5.6	
CD05	31.2	6.5	49.1	10.4	2.8			
CD08	15.4	7.8		5.7	2.2	68.9		
CD11	21.5	0.9		4.6		61.9	7.3	3.8
CD16	15.2	2.8	19.0	9.1	3.9	49.9		

3.2 Crystallographic Preferred Orientations

The crystallographic preferred orientations (CPOs) are shown in Figures 2a-2d. The CPOs are presented as contoured pole figures using the orientation distribution function (ODF) calculated with one point per grain for each mineral. The most abundant minerals in all samples can be grouped into quartz, feldspars, micas, and amphiboles, and the CPOs of these mineral groups are similar between the four rock types. The following discussion of mineral CPOs is organized by mineral group. Table 2a presents the ODF-J (a measure of CPO strength) averages and corresponding standard deviations of each mineral for each rock grouping. Table 2b presents the ODF-J for each sample and the number of grains (N) counted during EBSD analysis.

Table 2a. ODFJ averages with standard deviations for each mineral

	ODFJ Averages ± Standard Deviation					
	Quartz	Feldspar	Biotite	Muscovite	Chlorite	Hornblende
Felsic Gneiss	2.2 ± 0.7	2.7 ± 1.4	28.1 ± 12.6	9.6 ± 5.3	31.7 ± 13.4	19.4
Mafic Gneiss	2.3 ± 0.8	4.0 ± 2.2	29.9 ± 21.5	5.4 ± 1.3	81.4	8.1 ± 3.7
Felsic Schist	3.0 ± 1.9	12.5 ± 10.8	17.3 ± 6.1	7.9 ± 3.6	31.4	
Mafic Schist	2.0 ± 0.4	12.0 ± 8.5	11.6 ± 3.8	27.6 ± 38.5	13.7 ± 8.9	13.3 ± 10.3
Felsic	2.5 ± 1.0	6.8 ± 8.3	24.1 ± 11.7	8.9 ± 4.6	31.7 ± 11.0	19.4
Mafic	1.9 ± 0.6	7.6 ± 7.4	17.8 ± 16.9	18.6 ± 33.3	21.4 ± 28.8	9.5 ± 7.7
Gneiss	2.2 ± 0.7	3.2 ± 1.8	28.6 ± 14.4	8.7 ± 5.0	44.2 ± 27.1	10.3 ± 6.0
Schist	2.5 ± 1.0	12.2 ± 9.1	14.8 ± 5.7	17.7 ± 27.8	16.6 ± 10.8	13.3 ± 10.3

Table 2b. Number of grains indexed per mineral during EBSD and corresponding ODF-J values. Highlighted values are samples with low grain counts and high ODF-J values.

	Quartz		Feldspar		Biotite		Muscovite		Chlorite		Hornblende	
	N	ODFJ	N	ODFJ	N	ODFJ	N	ODFJ	N	ODFJ	N	ODFJ
Felsic Gneiss												
CD06	1520	1.8	2622	2.8	50	22.5	371	8.5	32	32.9		
CD07	2656	2.7	1559	2.9	30	47.8	167	19.3			433	19.4
CD15	7194	1.2	3250	1.9	189	13.6	1479	4.4	65	17.8		
CD19	2099	1.5	4148	1.8	557	18.4	321	6.5				
CD21	2846	3.0	4127	2.1	698	24.5	298	6.6				
CD22	6838	2.7	4822	1.8	1286	42.8	94	14.5				
CD27	3756	2.4	974	5.8	517	26.8	850	7.6	324	44.5		
Mafic Gneiss												
CD03	1627	3.0	1742	2.4							5425	6.5
CD10	1360	1.6	1083	3.0	150	8.5	413	4.4			5245	9.0
CD13	2224	3.1	5156	7.2	64	50.8			3501	81.4	13819	12.7
CD24	3082	1.6	1218	3.3	35	30.5	220.0	6.3			2097	4.0
Felsic Schist												
CD01	5042	2.4	4209	4.3	4091	25.3	5781	11.6				
CD09	1053	3.2	408	6.5	379	13.3	1112	4.8				
CD14	4364	2.2	1350	3.6	887	11.8	4063	4.7				
CD17	1011	2.2	249	20.9			234	12.0				
CD31	257	5.0	476	27.0	165	18.6	914	6.3	131	31.4		
Mafic Schist												
CD02	3240	2.3	2972	2.0	1252	10.0	938	5.6	1562	5.3	764	28.4
CD05	3467	1.4	352.0	10.5	1095	8.9	753	10.8	128	16.4		
CD08	781	2.1	117	24.6			61.0	20.1	40	27.9	3315	6.1
CD11	1483	1.9	426	8.1			49	95.7	319	8.6	3091	11.0
CD16	3340	2.5	276	14.8	1606	15.9	538	5.6	348	10.2	4340	7.6

3.2.1 Quartz

Quartz CPOs vary in strength, and are strongest in the felsic gneisses. ODF-J values range 1.2-3.0 in the felsic gneiss, 1.6-3.1 in the mafic gneiss, 2.2-5.0 in the felsic schist, and 1.4-2.5 in the mafic schist. Most of the quartz CPOs have concentrations of c-axes roughly perpendicular to the foliation. This is demonstrated by sample CD19 in Figure 2a. Sample CD21 displays (100) concentrations perpendicular to the foliation in a girdle that is also subparallel to the lineation.

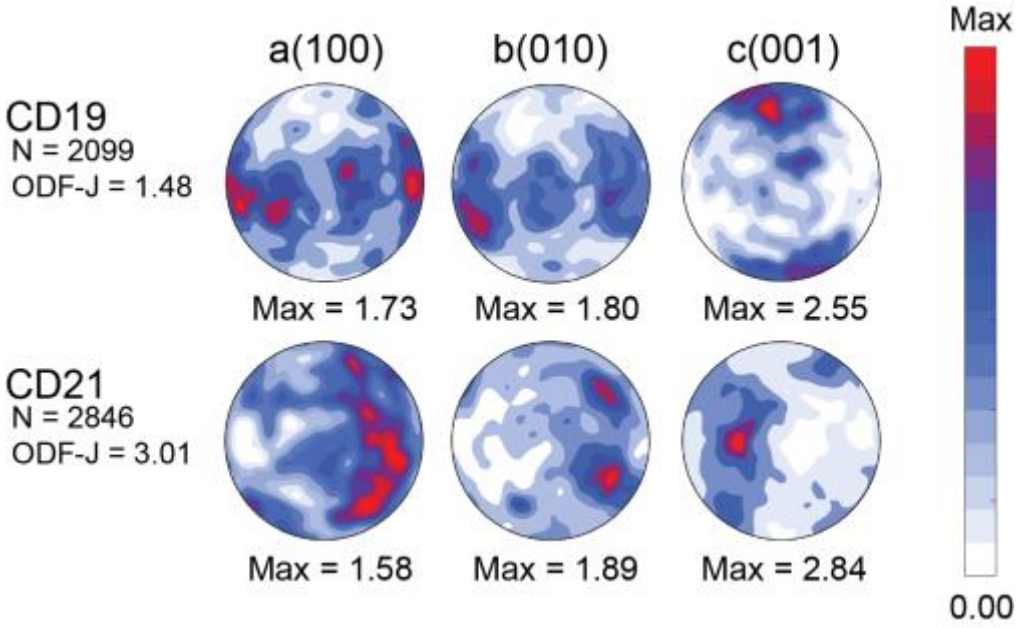

Figure 2a. Quartz CPOs for selected felsic gneiss samples

3.2.2 Feldspar Group (plagioclase)

Feldspar CPOs are visually the weakest in all rock types, as most of the samples do not have strong concentrations of any crystallographic direction. Two of the gneiss samples, shown in Figure 2b, do have apparent CPOs. CD03 has point concentrations of [010] perpendicular to the foliation and (001) parallel to the lineation. CD22 has point maxima of [010] subparallel to the lineation, and a girdle of (001) perpendicular to the lineation. Despite the visibly weak CPO, the ODF-J values are slightly higher than those for quartz, and range from 1.8 to 27.0.

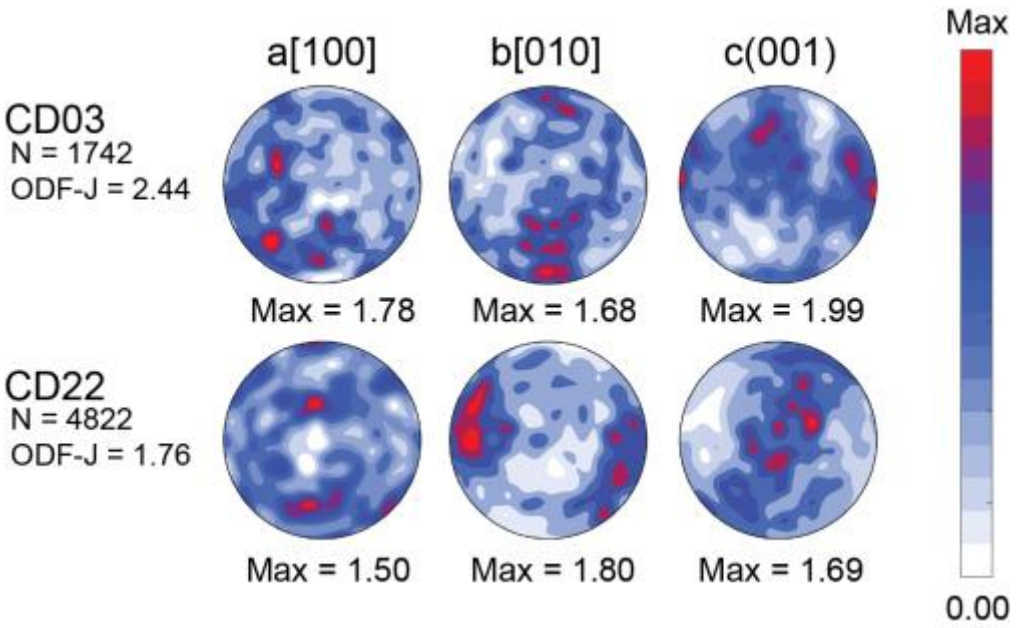

Figure 2b. Feldspar CPOs for gneiss samples

3.2.3 Mica Group (muscovite, biotite, chlorite)

Micas have the strongest CPO in all rock types when significant (>10%) mica is present, and the CPOs are strongest in the schists. The ODF-J values range 4.4-47.8 in felsic gneiss, 4.4-81.4 in mafic gneiss, 4.7-31.4 in felsic schist, and 5.3-95.7 in mafic schist. All of the micas, muscovite, biotite, and chlorite, have point concentrations of (001) poles perpendicular to the foliation (i.e. the 001 plane is parallel to the foliation). The biotite and chlorite CPOs have point concentrations of [100] parallel to the lineation (examples in Figure 2c., biotite-CD22 and chlorite-CD02). The muscovite CPOs display point concentrations of [100] subparallel to the lineation.

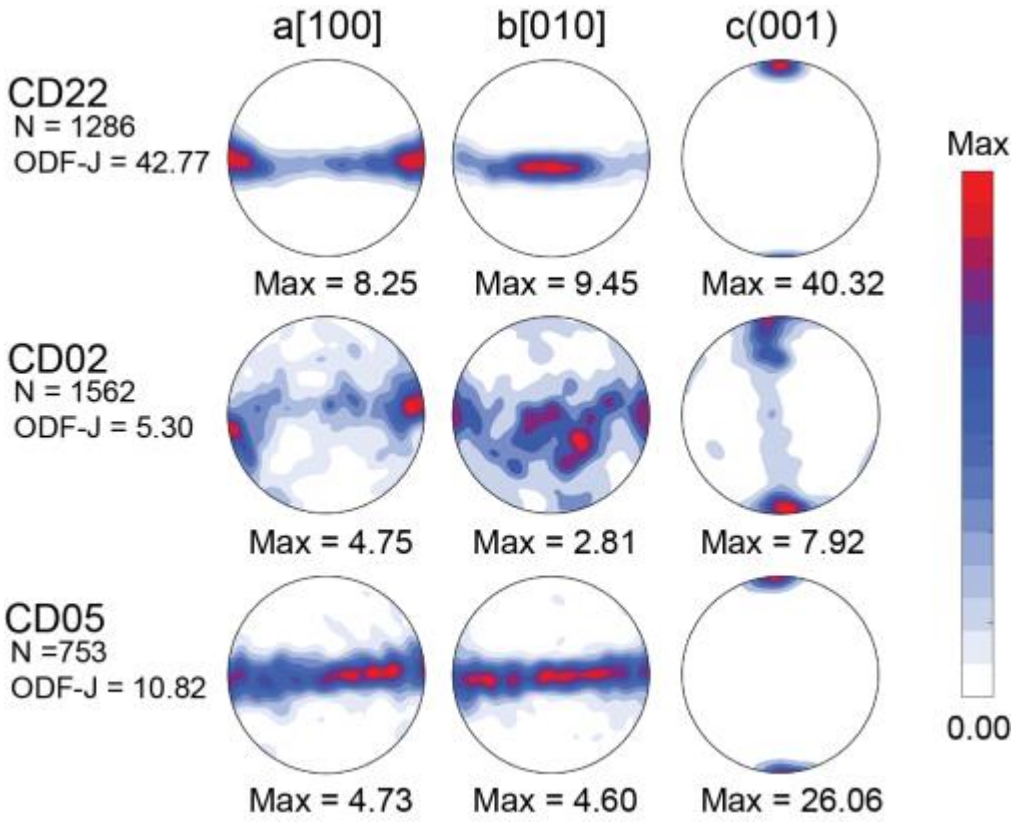

Figure 2c. Mica CPOs from top to bottom: biotite, chlorite, muscovite

3.2.4 Amphibole Group (hornblende)

The hornblende CPOs are weaker than the mica CPOs, but are strong when compared with the quartz and feldspar CPOs, and are the strongest in samples with significant (>10%) hornblende content. ODF-J values range 4.0-28.5. The mafic schists have the strongest hornblende CPOs with ODF-J values of 6.1-28.5. All of the hornblende-rich samples have a CPO with point concentrations of (100) perpendicular to the foliation, and [001] parallel to the lineation (Figure 2d). The sample with the weakest hornblende CPO, CD03, is slightly asymmetric relative to the foliation.

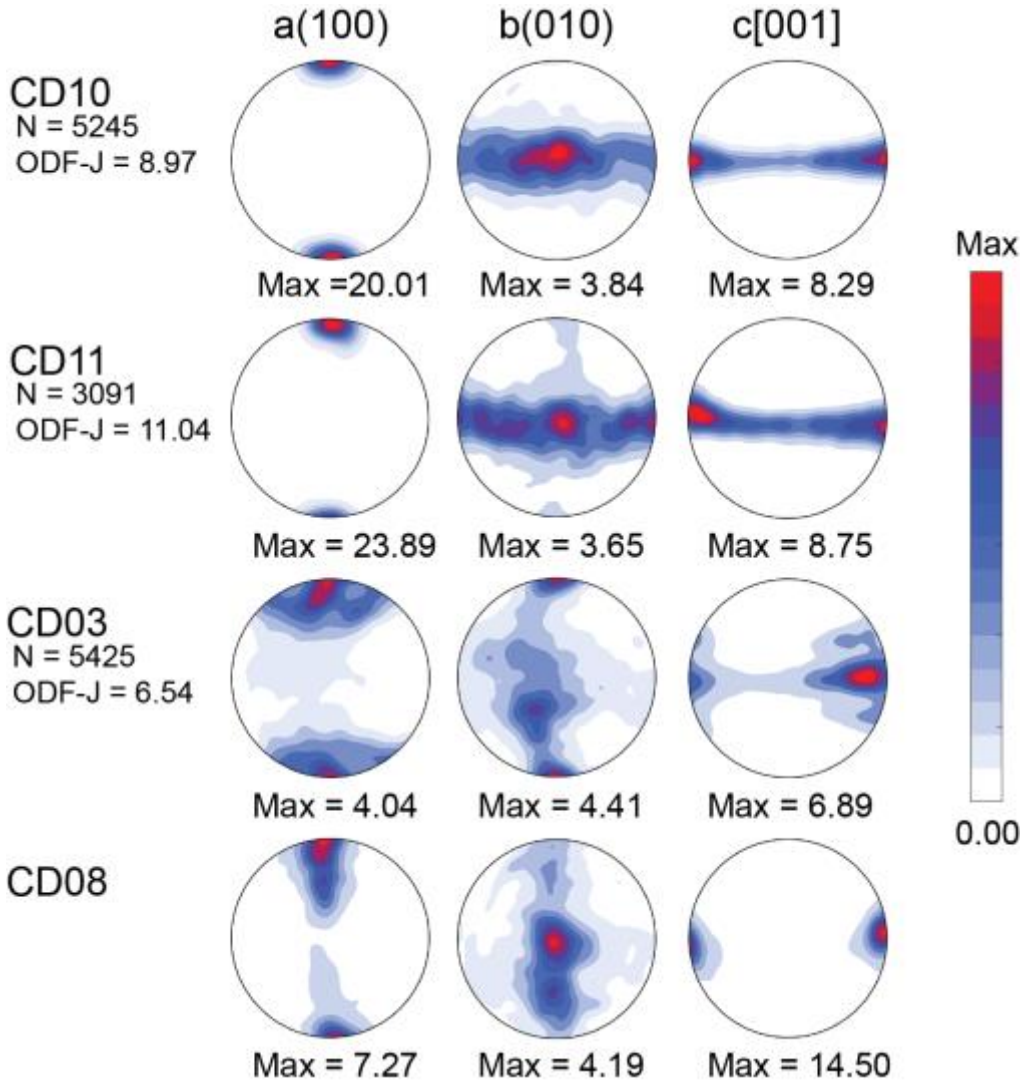

Figure 2d. Hornblende CPOs from mafic gneiss and schists

3.3 Elastic Tensor Calculations

Figures 3a and 3b display contoured stereonets of compressional wave velocity (Vp), the difference between the fast and slow shear wave velocities (DVs), and Vp/Vs. The seismic properties display variations that are related to rock type and composition. Table 3a reports the seismic properties for each sample, and Table 3b reports the averages for each rock group.

3.3.1 Isotropic seismic properties

Isotropic Vp ranges 5.6-6.5 km/s and is higher for the mafic rocks, although there is some overlap between the isotropic Vp in mafic and felsic groups with the felsic rocks averaging 6.0 ± 0.1 km/s and the mafic rocks averaging 6.3 ± 0.3 km/s. The gneiss and schist groups are almost identical averaging 6.1 ± 0.2 km/s in gneiss and 6.1 ± 0.3 km/s in schist. Isotropic Vs ranges 3.3-3.8 km/s and shows more variation than Vp. Isotropic Vp/Vs ranges 1.6-1.8 and is lowest in the felsic rocks, particularly those with high quartz content.

3.3.2 Seismic Anisotropy

Unlike the isotropic properties, seismic anisotropy varies more as a function of rock type than mafic or felsic composition, but variations are also observed between mafic and felsic rocks within rock types. For all samples, the slowest Vp is found for propagation perpendicular to the foliation, and the highest AVs is for propagation parallel to the foliation.

3.3.2.1 Gneiss anisotropy

Vp anisotropy in the gneisses ranges 4.0-14.8%, and is slightly higher in the mafic gneisses, although the two groups are within 1 standard deviation. AVs max is also very similar for both gneiss groups with values ranging 4.0-20.4% with the felsic gneisses having slightly higher maximum AVs averaging 13.2 ± 5.9 vs. 9.6 ± 3.5 in the mafic gneiss. The max Vp/Vs in the felsic gneisses is perpendicular to the foliation, and is parallel to the foliation in the mafic gneisses.

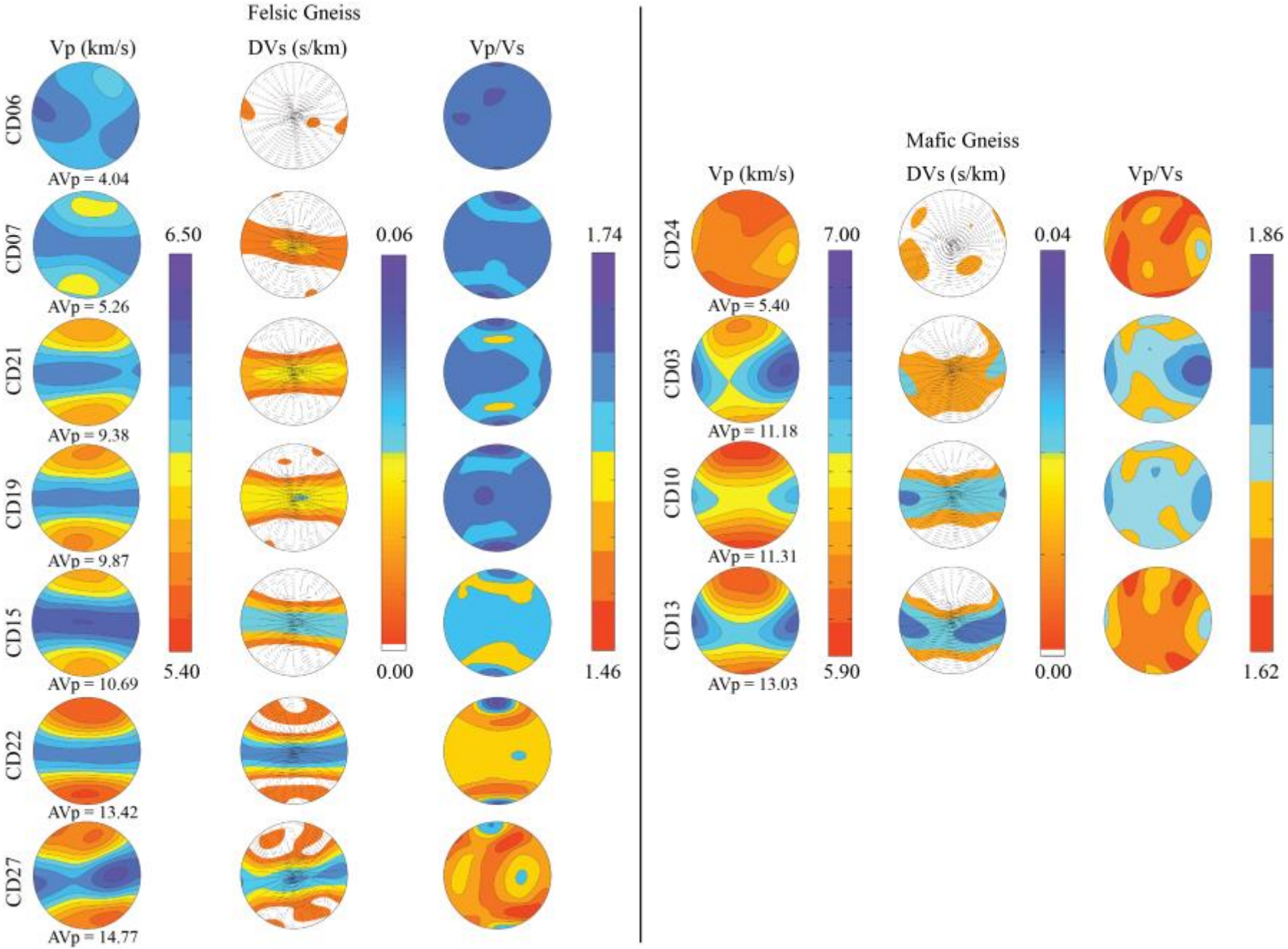

Figure 3a Contour plots for Vp, DVs, and VpVs for felsic gneiss and mafic gneiss

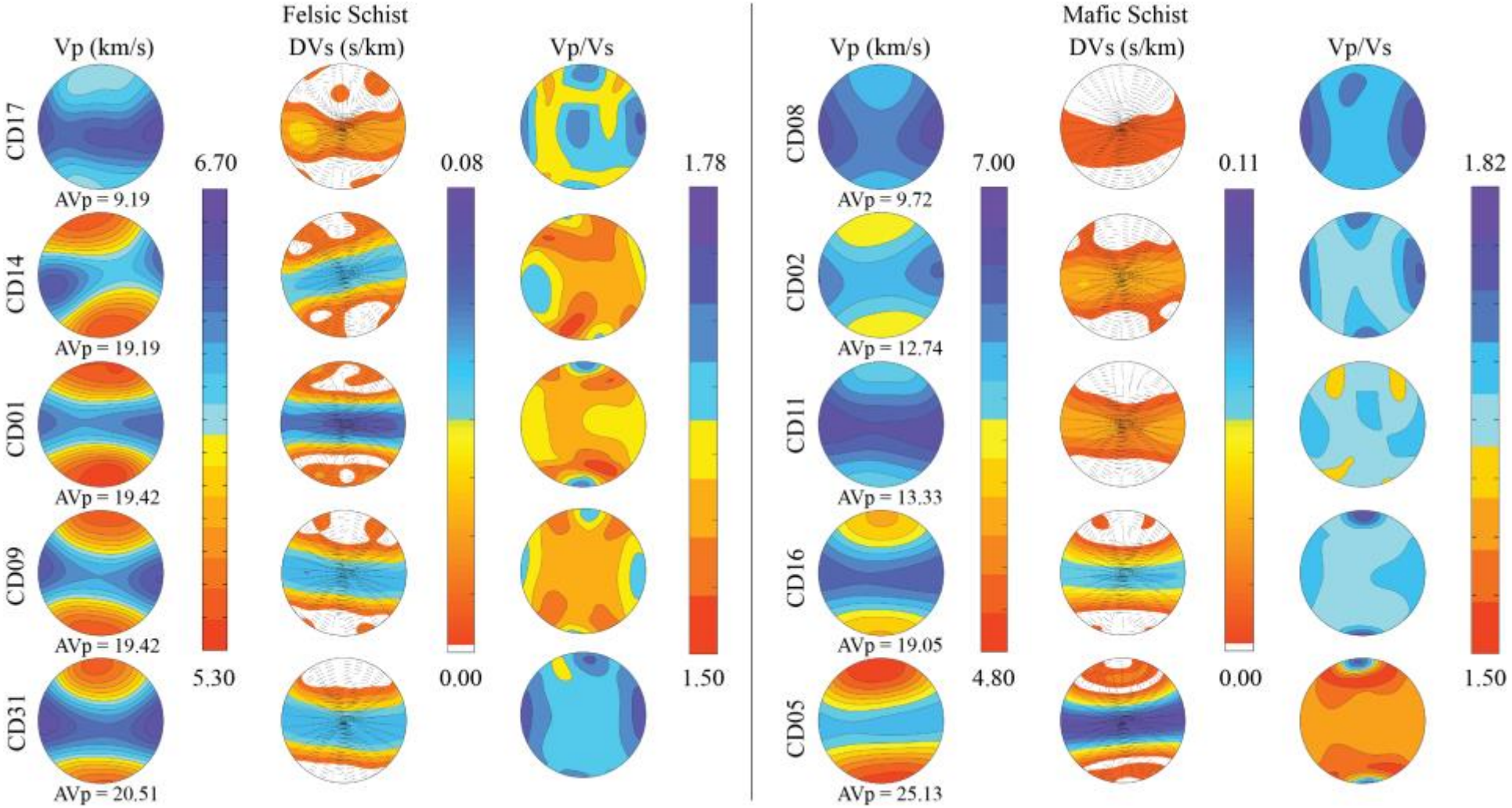

Figure 3b Contour plots for Vp, DVs, and VpVs for felsic schist and mafic schist

3.3.2.2 Schist anisotropy

Vp anisotropy in the schists is significantly higher than in the gneisses, and ranges 9.2-25.1%. The felsic schists have slightly higher AVp than the mafic schists, averaging 17.6 ± 4.7 in the felsic schist vs. 16.0 ± 6.1 in the mafic schist. AVs max ranges from 6.6-34.8% in the schists, and is also slightly higher in the felsic schist than the mafic schist, with a felsic average AVs of 20.2 ± 4.7 and a mafic average of 18.7 ± 11.1. The max of Vp/Vs in the felsic schists is typically parallel to the foliation, and is perpendicular to the foliation in the mafic schists.

3.3.3 Symmetry of Seismic Anisotropy

The symmetry of the calculated elastic tensors ranges from nearly hexagonal or transversely isotropic (TI), with one unique axis about which all velocities are symmetric, to having a significant component of orthorhombic symmetry, with 3 unique and orthogonal directions. These patterns are most easily visualized in the stereonet plots of Vp in Figures 3a and 3b. The patterns of Vp velocities suggest that in general mafic gneisses and schists are more orthorhombic than their felsic counter parts. Within the felsic groups, rocks containing more quartz are more orthorhombic than those with more feldspar. And within the mafic groups, rocks with more hornblende appear more orthorhombic in Vp symmetry. The shear wave anisotropy displays complicated patterns, but in general, AVs is mostly hexagonal in symmetry, with the lowest AVs found for propagation oblique to the symmetry axis, which is perpendicular to the foliation. So AVs is the lowest for propagation oblique to the foliation.

Table 3a. Seismic properties derived from calculated elastic tensors for individual samples with Voight and Ruess error bounds

	VpIso (km/s)	VsIso (km/s)	Vp/VsIso (km/s)	VpMin (km/s)	VpMax (km/s)	AVp (%)	Vs1Max (km/s)	AVsMax (%)
Felsic Gneiss								
CD06	$6.2^{-0.5}_{0.4}$	$3.6^{-0.3}_{0.3}$	$1.7^{0.0}_{0.0}$	$6.1^{-0.5}_{0.4}$	$6.3^{-0.5}_{0.5}$	$4.0^{0.1}_{0.0}$	$3.7^{-0.3}_{0.3}$	$4.0^{0.8}_{-0.3}$
CD07	$6.1^{-0.3}_{0.3}$	$3.6^{-0.2}_{0.2}$	$1.7^{0.0}_{0.0}$	$6.0^{-0.3}_{0.3}$	$6.3^{-0.4}_{0.3}$	$5.3^{-0.1}_{0.3}$	$3.7^{-0.2}_{0.2}$	$8.0^{0.9}_{-0.7}$
CD15	$6.1^{-0.5}_{0.5}$	$3.6^{-0.4}_{0.4}$	$1.7^{0.0}_{0.0}$	$5.8^{-0.5}_{0.5}$	$6.4^{-0.4}_{0.4}$	$10.7^{0.5}_{-0.3}$	$3.9^{-0.4}_{0.3}$	$14.3^{4.0}_{-2.6}$
CD19	$6.0^{-0.4}_{0.4}$	$3.5^{-0.3}_{0.3}$	$1.7^{0.1}_{0.0}$	$5.7^{-0.4}_{0.3}$	$6.3^{-0.4}_{0.4}$	$9.9^{0.6}_{-0.2}$	$3.7^{-0.3}_{0.3}$	$13.9^{4.4}_{-3.0}$
CD21	$6.0^{-0.4}_{0.4}$	$3.5^{-0.3}_{0.3}$	$1.7^{0.0}_{0.0}$	$5.7^{-0.4}_{0.4}$	$6.3^{-0.4}_{0.4}$	$9.4^{0.5}_{-0.1}$	$3.7^{-0.3}_{0.3}$	$12.3^{2.9}_{-1.9}$
CD22	$5.9^{-0.4}_{0.4}$	$3.5^{-0.4}_{0.4}$	$1.7^{0.1}_{0.0}$	$5.5^{-0.4}_{0.4}$	$6.3^{-0.4}_{0.4}$	$13.4^{1.3}_{-0.5}$	$3.9^{-0.3}_{0.3}$	$20.4^{8.7}_{-5.5}$
CD27	$5.9^{-0.5}_{0.4}$	$3.7^{-0.4}_{0.4}$	$1.6^{0.1}_{0.0}$	$5.6^{-0.4}_{0.4}$	$6.4^{-0.4}_{0.4}$	$14.8^{1.6}_{-1.0}$	$4.1^{-0.3}_{0.3}$	$19.7^{7.2}_{-4.8}$
Mafic Gneiss								
CD03	$6.5^{-0.3}_{0.3}$	$3.6^{-0.3}_{0.2}$	$1.8^{0.0}_{0.0}$	$6.2^{-0.2}_{0.2}$	$6.9^{-0.3}_{0.3}$	$11.2^{-0.8}_{0.8}$	$3.8^{-0.1}_{0.2}$	$8.0^{1.4}_{-0.4}$
CD10	$6.3^{-0.4}_{0.4}$	$3.5^{-0.3}_{0.3}$	$1.8^{0.0}_{0.0}$	$5.9^{-0.4}_{0.3}$	$6.6^{-0.4}_{0.3}$	$11.3^{-1.55}_{1.22}$	$3.7^{-0.3}_{0.3}$	$11.1^{-0.1}_{0.3}$
CD13	$6.4^{-0.3}_{0.3}$	$3.7^{-0.2}_{0.2}$	$1.7^{0.0}_{0.0}$	$6.0^{-0.3}_{0.2}$	$6.8^{-0.3}_{0.3}$	$12.5^{-0.55}_{0.80}$	$3.9^{-0.2}_{0.2}$	$13.6^{1.5}_{-0.9}$
CD24	$6.1^{-0.4}_{0.4}$	$3.6^{-0.3}_{0.3}$	$1.7^{0.0}_{0.0}$	$6.0^{-0.4}_{0.4}$	$6.3^{-0.5}_{0.4}$	$5.4^{-0.24}_{0.38}$	$3.7^{-0.3}_{0.3}$	$5.6^{1.2}_{-0.6}$
Felsic Schist								
CD01	$5.9^{-0.5}_{0.5}$	$3.5^{-0.4}_{0.4}$	$1.7^{0.1}_{-0.1}$	$5.3^{-0.4}_{0.4}$	$6.5^{-0.5}_{0.5}$	$19.4^{0.2}_{0.2}$	$3.9^{-0.4}_{0.4}$	$25.7^{5.9}_{-3.6}$
CD09	$6.0^{-0.6}_{0.6}$	$3.6^{-0.5}_{0.4}$	$1.7^{0.1}_{0.0}$	$5.4^{-0.5}_{0.5}$	$6.6^{-0.6}_{0.6}$	$19.4^{0.5}_{-0.3}$	$4.0^{-0.4}_{0.4}$	$21.4^{6.3}_{-3.7}$
CD14	$5.9^{-0.5}_{0.5}$	$3.5^{-0.4}_{0.4}$	$1.7^{0.1}_{0.0}$	$5.4^{-0.5}_{0.4}$	$6.6^{-0.5}_{0.5}$	$19.2^{0.7}_{-0.3}$	$3.9^{-0.4}_{0.4}$	$20.3^{5.4}_{-3.4}$
CD17	$6.3^{-0.5}_{0.5}$	$3.7^{-0.3}_{0.3}$	$1.7^{0.0}_{0.0}$	$6.1^{-0.5}_{0.5}$	$6.6^{-0.5}_{0.5}$	$9.2^{1.1}_{-0.7}$	$3.9^{-0.3}_{0.3}$	$12.8^{1.9}_{-1.3}$
CD31	$6.1^{-0.6}_{0.6}$	$3.4^{-0.5}_{0.4}$	$1.8^{0.1}_{-0.1}$	$5.5^{-0.5}_{0.4}$	$6.7^{-0.6}_{0.6}$	$20.5^{-0.7}_{0.6}$	$3.9^{-0.5}_{0.4}$	$20.7^{4.0}_{-2.2}$
Mafic Schist								
CD02	$6.2^{-0.6}_{0.5}$	$3.5^{-0.5}_{0.4}$	$1.8^{0.1}_{0.0}$	$5.8^{-0.6}_{0.5}$	$6.6^{-0.6}_{0.5}$	$12.7^{0.7}_{-0.3}$	$3.8^{-0.4}_{0.4}$	$14.2^{5.8}_{-3.6}$
CD05	$5.6^{-0.7}_{0.6}$	$3.3^{-0.6}_{0.5}$	$1.7^{0.2}_{-0.1}$	$4.9^{-0.5}_{0.4}$	$6.3^{-0.7}_{0.7}$	$25.1^{-2.5}_{2.1}$	$3.9^{-0.6}_{0.5}$	$34.8^{10.2}_{-4.9}$
CD08	$6.5^{-0.3}_{0.3}$	$3.7^{-0.1}_{0.1}$	$1.8^{0.0}_{0.0}$	$6.3^{-0.2}_{0.2}$	$6.9^{-0.3}_{0.3}$	$9.7^{-1.2}_{1.1}$	$3.8^{-0.1}_{0.1}$	$6.6^{-0.1}_{0.3}$
CD11	$6.5^{-0.3}_{0.3}$	$3.8^{-0.2}_{0.2}$	$1.7^{0.0}_{0.0}$	$6.1^{-0.3}_{0.3}$	$7.0^{-0.4}_{0.3}$	$13.3^{-0.8}_{0.7}$	$4.1^{-0.2}_{0.2}$	$13.3^{1.4}_{-0.6}$
CD16	$6.2^{-0.5}_{0.5}$	$3.5^{-0.4}_{0.3}$	$1.8^{0.1}_{0.0}$	$5.6^{-0.4}_{0.3}$	$6.8^{-0.5}_{0.5}$	$19.1^{-0.9}_{0.9}$	$3.9^{-0.3}_{0.3}$	$24.7^{7.0}_{-4.6}$

Table 3b. Averages of seismic properties derived from the calculated elastic tensors

	Average ± Standard Deviation							
	VpIso (km/s)	VsIso (km/s)	Vp/VsIso (km/s)	VpMin (km/s)	VpMax (km/s)	AVp (%)	Vs1Max (km/s)	AVsMax (%)
Felsic Gneiss	6.0 ± 0.1	3.6 ± 0.1	1.7 ± 0.0	5.8 ± 0.2	6.3 ± 0.1	9.6 ± 3.9	3.8 ± 0.1	13.2 ± 5.9
Mafic Gneiss	6.3 ± 0.2	3.6 ± 0.1	1.8 ± 0.1	6.0 ± 0.1	6.7 ± 0.3	10.1 ± 3.2	3.8 ± 0.1	9.6 ± 3.5
Felsic Schist	6.0 ± 0.1	3.5 ± 0.1	1.7 ± 0.0	5.5 ± 0.3	6.6 ± 0.1	17.6 ± 4.7	3.9 ± 0.1	20.2 ± 4.7
Mafic Schist	6.2 ± 0.4	3.5 ± 0.2	1.8 ± 0.0	5.7 ± 0.5	6.7 ± 0.3	16.00 ± 6.1	3.9 ± 0.1	18.7 ± 11.1
Felsic	6.0 ± 0.1	3.6 ± 0.1	1.7 ± 0.0	5.7 ± 0.3	6.4 ± 0.2	12.9 ± 5.8	3.9 ± 0.1	16.1 ± 6.3
Mafic	6.3 ± 0.3	3.6 ± 0.2	1.8 ± 0.0	5.9 ± 0.4	6.7 ± 0.2	13.4 ± 5.7	3.9 ± 0.1	14.7 ± 9.4
Gneiss	6.1 ± 0.2	3.6 ± 0.1	1.7 ± 0.0	5.9 ± 0.2	6.5 ± 0.2	9.8 ± 3.5	3.8 ± 0.1	11.9 ± 5.3
Schist	6.1 ± 0.3	3.5 ± 0.2	1.7 ± 0.0	5.6 ± 0.4	6.7 ± 0.2	16.8 ± 5.2	3.9 ± 0.1	19.5 ± 8.0

3.3.3.1 Tensor Symmetry Decomposition

The elastic tensors were decomposed into their symmetry components in order to quantify contributions of different symmetries to the total tensor (Table 6). The most important symmetry components in all samples are hexagonal, orthorhombic, and triclinic. The triclinic component in this decomposition is the remaining tensor after removing the isotropic, hexagonal, tetragonal, orthorhombic, and monoclinic components, in that order. There were symmetry components that we did not remove, e.g. trigonal, so the triclinic component may yet have some symmetry. There are some patterns with respect to rock type and symmetry.

The gneisses have the highest isotropic component on average, with the felsic gneisses having a higher isotropic component on average than the mafic gneisses. Felsic and mafic gneisses have similarly high hexagonal components of the total elastic tensor, ranging from 1.5-13.1%. However, if we remove the isotropic component, and only focus on the anisotropy, the mafic

gneisses have slightly lower hexagonal (57.0 ± 16.5%), and slightly higher orthorhombic (21.1 ± 11.0%) components of anisotropy than the felsic gneisses.

Table 4. The components of calculated elastic tensors listed as a percentage of the overall anisotropy of the given sample

Calculated Elastic Tensors (%)						
	Anisotropic	Hexagonal	Orthogonal	Tetragonal	Monoclinic	Triclinic
Felsic Gneiss						
CD06	3.1	47.9	15.7	0.6	2.0	33.7
CD07	5.4	77.9	7.7	0.1	1.1	13.2
CD15	10.7	89.6	1.2	0.1	1.7	7.4
CD19	11.0	55.6	0.8	0.2	0.0	43.3
CD21	9.2	84.2	3.6	0.2	7.0	5.0
CD22	14.7	89.0	0.2	0.0	1.9	8.9
CD27	14.5	75.7	9.7	0.2	5.7	8.7
Mafic Gneiss						
CD03	8.1	46.0	36.8	0.0	2.2	15.0
CD10	8.8	74.4	13.5	0.6	0.4	11.1
CD13	10.4	67.6	20.3	0.3	3.9	7.9
CD24	4.0	40.2	13.8	1.4	11.3	33.3
Felsic Schist						
CD01	18.6	84.3	3.2	0.0	4.6	7.8
CD09	16.9	77.7	15.4	0.7	0.2	6.0
CD14	16.2	69.6	21.7	0.5	2.6	5.6
CD17	8.4	67.1	4.8	0.2	12.1	15.8
CD31	16.4	80.2	11.5	0.4	1.2	6.7
Mafic Schist						
CD02	10.5	65.4	26.8	1.5	0.3	5.9
CD05	25.0	93.5	2.3	0.1	0.0	4.1
CD08	7.1	48.5	38.5	0.5	2.8	9.8
CD11	11.2	81.9	6.7	0.1	1.3	10.0
CD16	17.7	91.5	6.0	0.0	1.0	1.5
Average ± Standard Deviation						
Felsic Gneiss	9.8 ± 4.3	74.3 ± 16.4	5.6 ± 5.8	0.2 ± 0.2	2.8 ± 2.6	17.2 ± 15.0
Mafic Gneiss	7.8 ± 2.7	57.0 ± 16.5	21.1 ± 10.9	0.6 ± 0.6	4.5 ± 4.8	16.8 ± 11.3
Felsic Schist	15.3 ± 3.9	75.8 ± 7.2	11.3 ± 7.6	0.3 ± 0.3	4.2 ± 4.8	8.4 ± 4.2
Mafic Schist	14.3 ± 7.1	76.2 ± 19.0	16.1 ± 15.8	0.4 ± 0.6	1.1 ± 1.1	6.3 ± 3.7
Felsic	12.1 ± 4.9	74.9 ± 12.9	8.0 ± 6.9	0.3 ± 0.2	3.4 ± 3.5	13.5 ± 12.3
Mafic	11.4 ± 6.3	67.7 ± 19.6	18.3 ± 13.3	0.5 ± 0.6	2.6 ± 3.5	11.0 ± 9.3
Gneiss	9.1 ± 3.8	68.0 ± 17.8	11.2 ± 10.8	0.3 ± 0.4	3.4 ± 3.4	17.1 ± 13.2
Schist	14.8 ± 5.5	76.0 ± 13.6	13.7 ± 12.0	0.4 ± 0.5	2.6 ± 3.6	7.3 ± 3.9

The schists have lower isotropic components of the total tensor, and higher hexagonal components of anisotropy than the gneisses. Comparing only the anisotropic components, the

hexagonal component of both the felsic and mafic schists are within 1 standard deviation of each other. The orthorhombic component is slightly higher in the mafic schists (16.1 ± 15.8%) than the felsic schists (11.3 ± 7.6%).

In viewing the Vp plots in Figure 3a, all of the felsic gneiss samples appear to be mostly hexagonal with a slow unique axis perpendicular to the foliation. Many of the samples have a minor orthorhombic component that is visible as a velocity maximum within the plane of fast velocities. CD27 has a more visibly orthorhombic elastic tensor, while CD06 appears more triclinic, with little to no symmetry behavior. The mafic gneisses are also approximately hexagonal, but have a larger orthorhombic component. CD03 and CD13 are mostly orthorhombic, and CD13 is the more hexagonal of the two. This difference is most likely due to the higher amounts of hornblende in CD03 and quartz in CD13. CD24 appears more orthorhombic, and is less anisotropic than the other samples, which may be related to thicker gneissic banding in this sample.

From the Vp plots in Figure 3b, the felsic schist group is very hexagonal with a strong orthorhombic component. CD01, CD09 and CD31 are more anisotropic and hexagonal than the other samples. CD17 is the least anisotropic sample. The mafic schist samples are less anisotropic and have the same combination of hexagonal and orthorhombic symmetry, with the exception of CD02 and CD08, which appear mostly orthorhombic. CD11 is more triclinic than CD17. CD31 is the most anisotropic and hexagonal of the group. Sample CD05 is the most anisotropic sample due to its high biotite content.

When comparing Figures 3a and 3b, the mafic rocks are more orthorhombic than the felsic rocks, which are mostly hexagonal. The felsic schists are more hexagonal than the felsic gneisses,

and the mafic gneisses are visibly more orthorhombic than the mafic schists. Generally, schists are more anisotropic than gneisses because of the mica content.

Chapter 4: Discussion

4.1 Mineralogy vs Elastic Tensors and Seismic Anisotropy

Figures 4a-7a show the relationship of a given mineral to the anisotropy of the elastic tensor for each sample. Figures 4b-7b show the relationship of a mineral to the symmetry component that the mineral affects the most. Quartz and hornblende are expected to affect the orthorhombic component, while mica will affect the hexagonal component. Feldspar does not generally affect a specific anisotropic component, but is expected to make a tensor more isotropic.

4.1.1 Hypothesis 1

Samples with more quartz will decrease overall anisotropy, and increase the orthorhombic symmetry component. As seen in Figure 4.1b, the felsic gneisses have a positive correlation between the modal quartz content and the orthorhombic component of the elastic tensors. The felsic schist may also have a steeper trend than the felsic gneiss if sample CD09 is treated as an outlier. Because the mafic schists have a larger range in quartz than the felsic schist, they display a very rapid increase in anisotropy with relation to quartz content (Figure 4a). This is likely caused by the content of hornblende and mica in the mafic schist. The mafic gneisses do not have a strong trend, positive or negative, with anisotropy, but the orthorhombic component generally decreases when there is less quartz present.

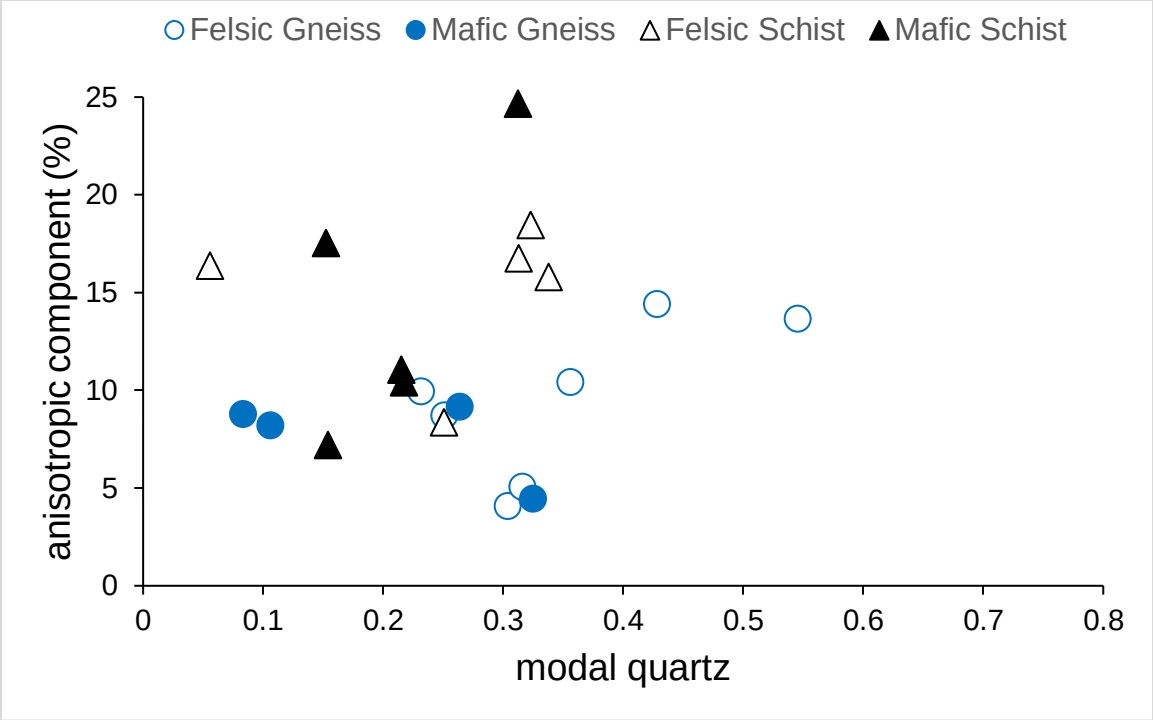

Figure 4a. Modal quartz content versus anisotropic component of the elastic tensor for each sample

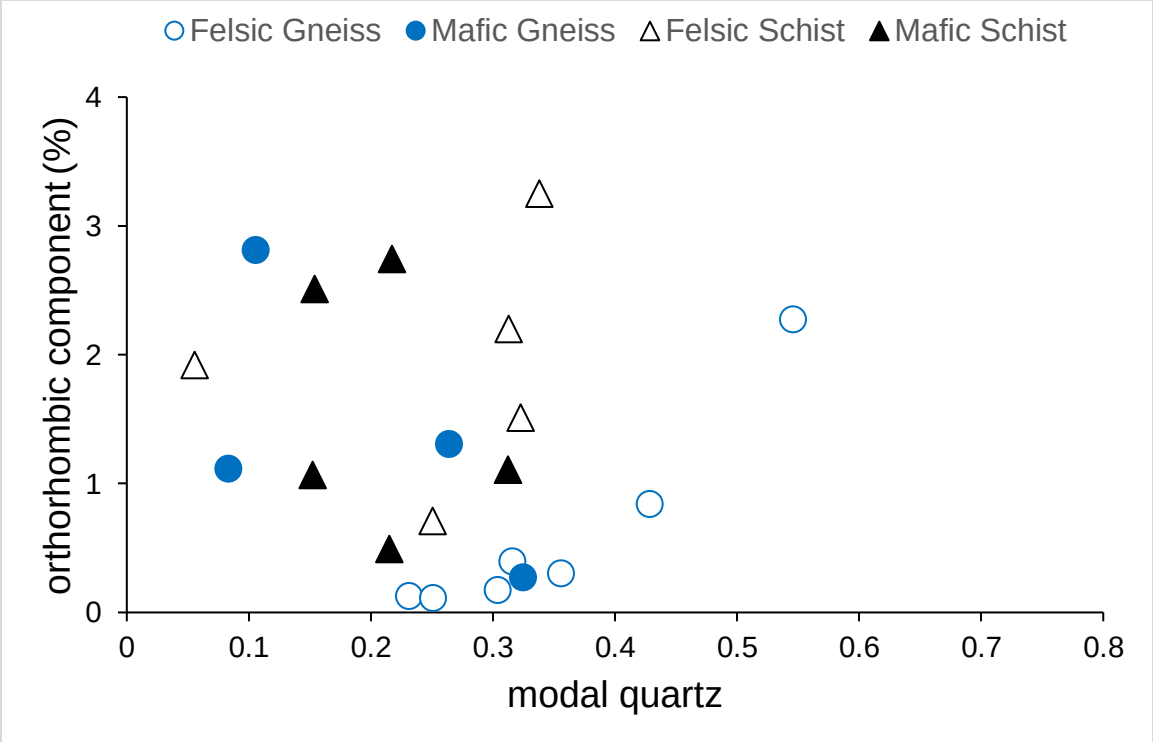

Figure 4b. Modal quartz content versus the orthorhombic component of the elastic tensor for each sample

Almost every rock group shows a negative correlation between modal feldspar content and the anisotropy of the elastic tensor (Figure 5a) or a positive correlation with isotropy. In Figure 5b there appears to be a positive trend between the feldspar content and the orthorhombic component in the mafic schist. Similar to the mafic schist trends in 4b, this is likely caused by the hornblende content. The felsic gneiss samples are the least anisotropic group because of their high feldspar contents. Generally, the presence of feldspar lowers anisotropy.

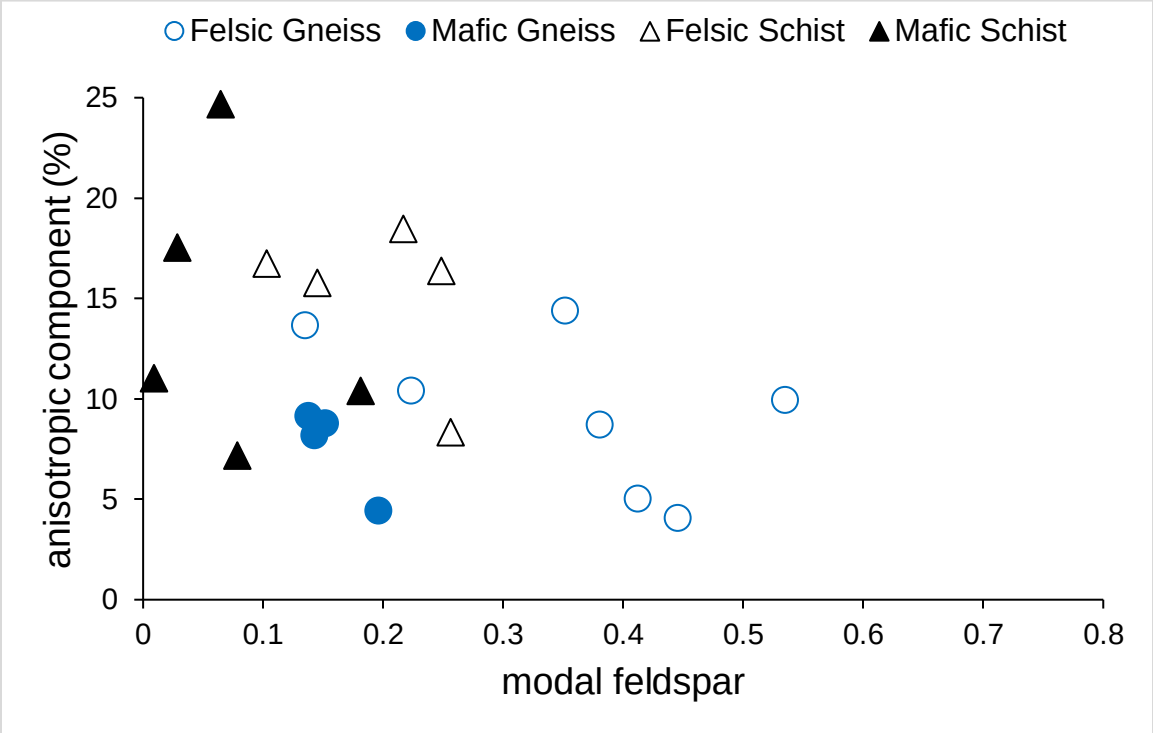

Figure 5a. Modal feldspar content versus anisotropic component of the elastic tensor for each sample

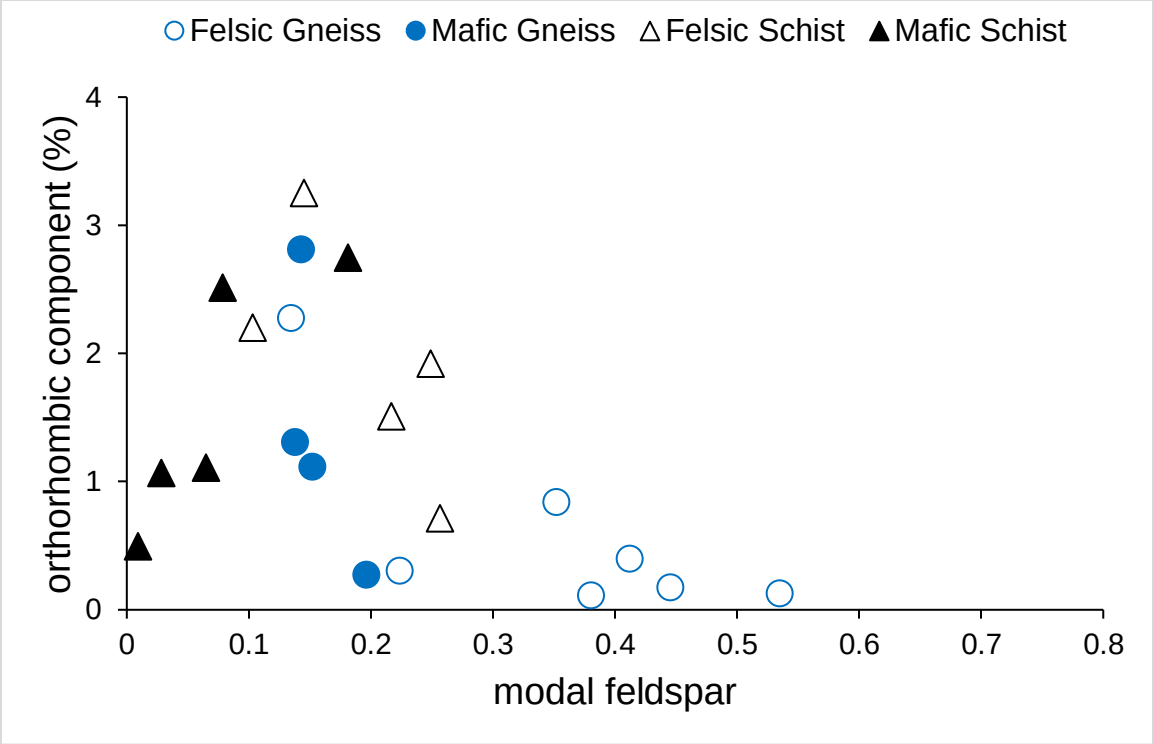

Figure 5b. Modal feldspar content versus the orthorhombic component of the elastic tensor for each sample

4.1.2 Hypothesis 2

Mica will increase anisotropy and the hexagonal symmetry component. Within each rock type grou, there is no distinct correlation between modal mica and magnitude of anisotropy. However, when looking at all the samples, there is a clear positive correlation between mica content and anisotropy. The link between mica contents and anisotropy has been documented in recent studies (Shao et al., 2016; Ward et al., 2012). The samples also display a positive correlation between the hexagonal symmetry component and mica content (Figure 6b). Both felsic and mafic schists have the most distinct trends, with the hexagonal symmetry component being closely related to modal mica contents.

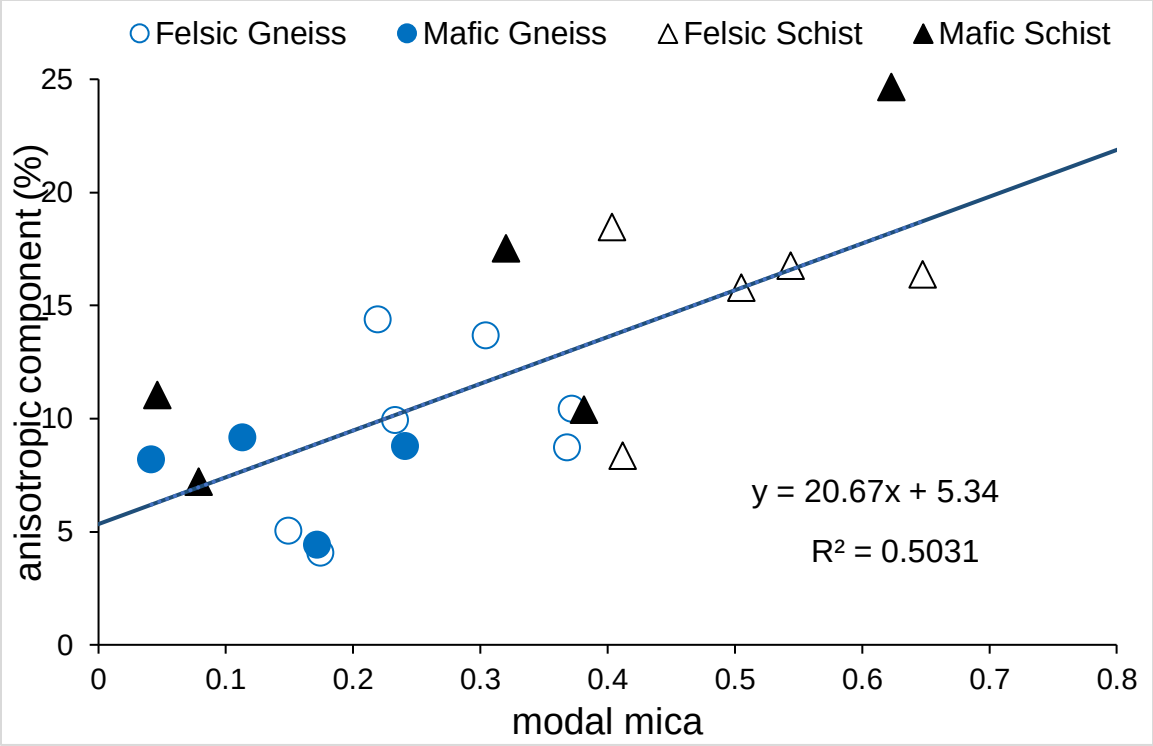

Figure 6a. Modal mica content versus anisotropic component of the elastic tensor for each sample

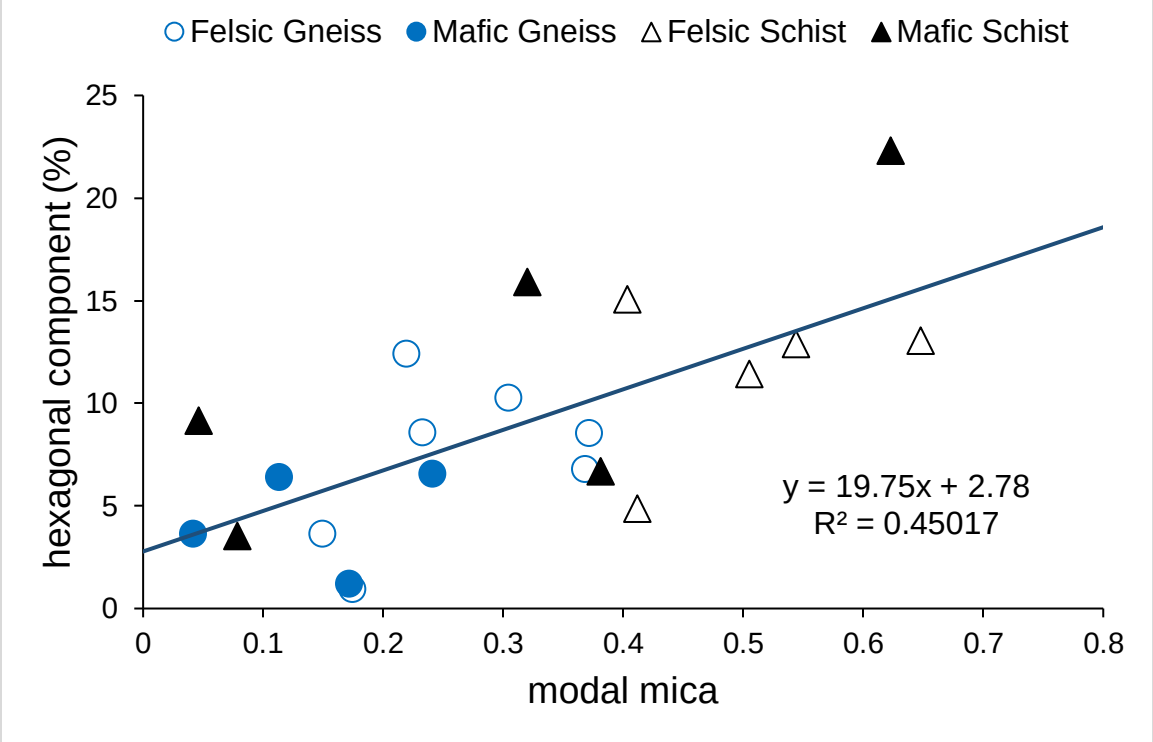

Figure 6b. Modal mica content versus the hexagonal component of the elastic tensor for each sample

4.1.3 Hypothesis 3

Amphibole will increase the magnitude of anisotropy and the orthorhombic symmetry component. There is a positive correlation between the orthorhombic symmetry component and hornblende content in both mafic groups, if CD02 (a mafic schist sample) is considered an outlier. This sample has high quartz content, lower total anisotropy, and thus the orthorhombic component is apparently higher despite low hornblende content. In both Figures 7a and 7b, the mafic gneisses have a clearer trend than the mafic schist. This may be caused by the varying mica contents in the mafic schist, with some containing ~50% biotite, which would add to the hexagonal component instead of the orthorhombic component, and would also explain why the mafic schists are more anisotropic.

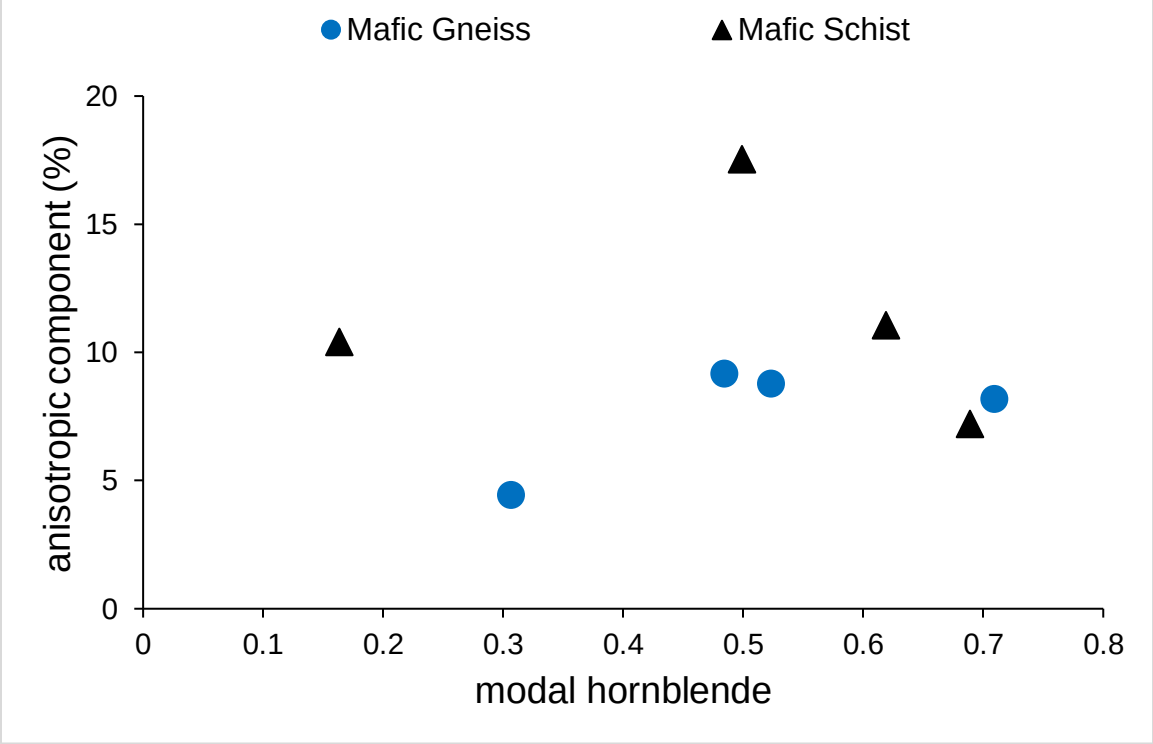

Figure 7a. Modal hornblende content versus anisotropic component of the elastic tensor for the mafic rock groups

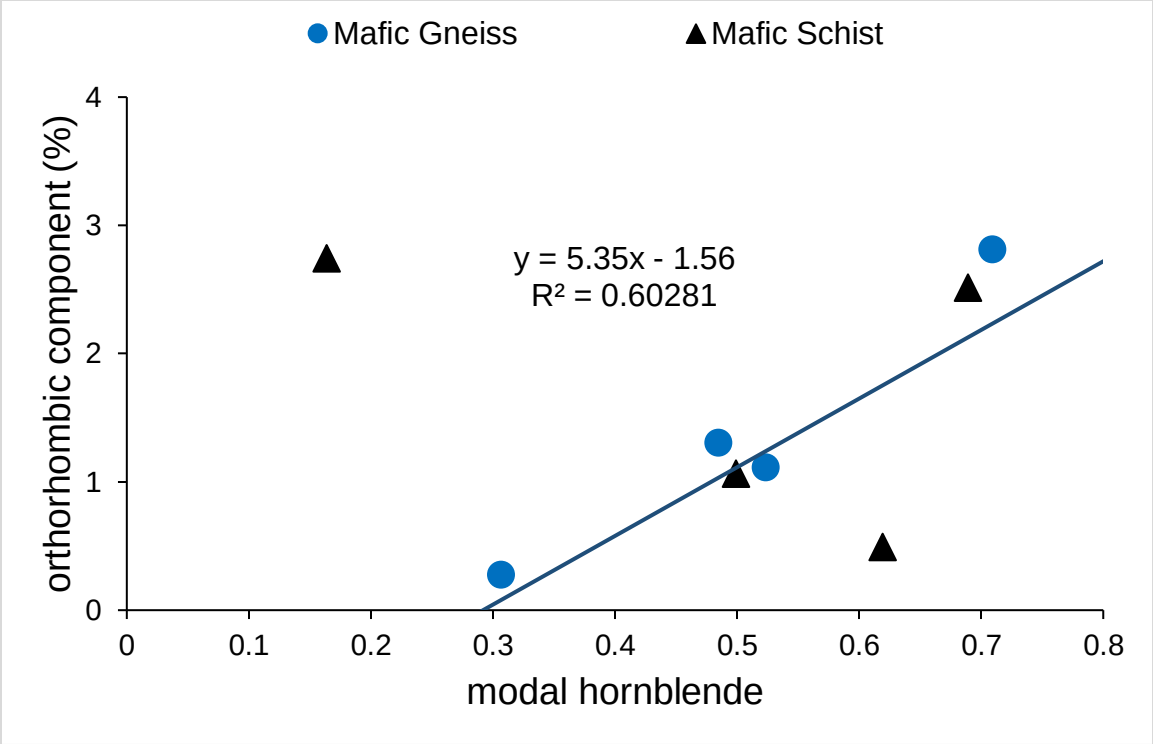

Figure 7b. Modal hornblende content versus the orthorhombic component of the elastic tensor for the mafic rock groups

4.2 CPOs

4.2.1 Quartz

The quartz CPOs that display high concentrations of [0001] perpendicular to the foliation (CD19 in Figure 2a) are consistent with the basal <a> slip system. The quartz CPOs that display c-axis concentrations almost parallel to the foliation also generally have a cross-girdle, which is consistent with a combination of basal <a> and prism <a> slip (CD21, Figure 2a). Previous studies (Kruhl, 1996) have shown that samples containing basal-<a> slip experience deformation processes at lower temperatures than samples with prism <a> slip. CD19 has a stronger and more distinct CPO than CD21, which suggests dominance of one slip system over any other, and contributes to CD19 being more anisotropic than CD21.

4.2.2 Feldspar Group (plagioclase)

Sample CD03 displays point maxima of (010) perpendicular to the foliation, and [001] parallel to lineation, which is consistent with slip on the (010) plane in the direction of [001]. The (010) [001] slip system is one of the most dominant slip systems in plagioclase feldspar (Olsen and Kohlstedt, 1984; Ji and Mainprice, 1988). CD22 displays a CPO consistent with slip along (001) in the [010] direction. There are studies that refer to (001) [010] as a slip system for feldspar (Olsen and Kohlstedt, 1984), but feldspar slip systems are not well understood because feldspar tends to deform by brittle deformation mechanisms in laboratory experiments.

4.2.3 Mica Group (muscovite, biotite, chlorite)

All of the mica CPOs are consistent with slip along (001) in the [100] direction. This is the most documented slip system for mica (e.g. Aleksandrov and Ryzhova, 1961). Biotite and muscovite display stronger CPOs than chlorite. The chlorite CPOs are weaker, likely due to lower grain counts, and because the chlorite is probably an alteration product of garnet (Karabinos, 2002), and thus its CPO is determined by reaction crystallization rather than deformation.

4.2.4 Amphibole Group (hornblende)

Hornblende CPOs are generally consistent with slip on (100) in the [001] direction, which is the typical slip system for hornblende deforming in simple shear (Hacker and Christie, 1990). In CD11, the point concentrations in (010) are stretched into a weak cross-girdle. CD03 displays a stronger cross-girdle in (010), and a cross-girdle is present in (100) as well, along with a stronger point concentration of [001]. CD08 has strong point concentrations of [001] and strong girdles of (010) and (100). This pattern in the distribution of crystallographic orientations is found in constrictional deformation (Lloyd et al., 2011).

4.3 Patterns of Velocity Stereonets

4.3.1 Vp Patterns

The Vp velocity stereonets in Figures 3a and 3b all have interesting patterns within the rock groups, and these patterns can be related back to single mineral elastic properties. The Vp velocity stereonets for single mineral tensors are shown in Figure 8. The felsic schist, mafic schist, and a few felsic gneiss samples all have similar Vp patterns where the fastest velocity is parallel to the lineation and there is no apparent orthorhombic component. This is associated with the mica Vp stereonets (bottom row of Fig. 8). Most of the samples with this pattern also have high anisotropy.

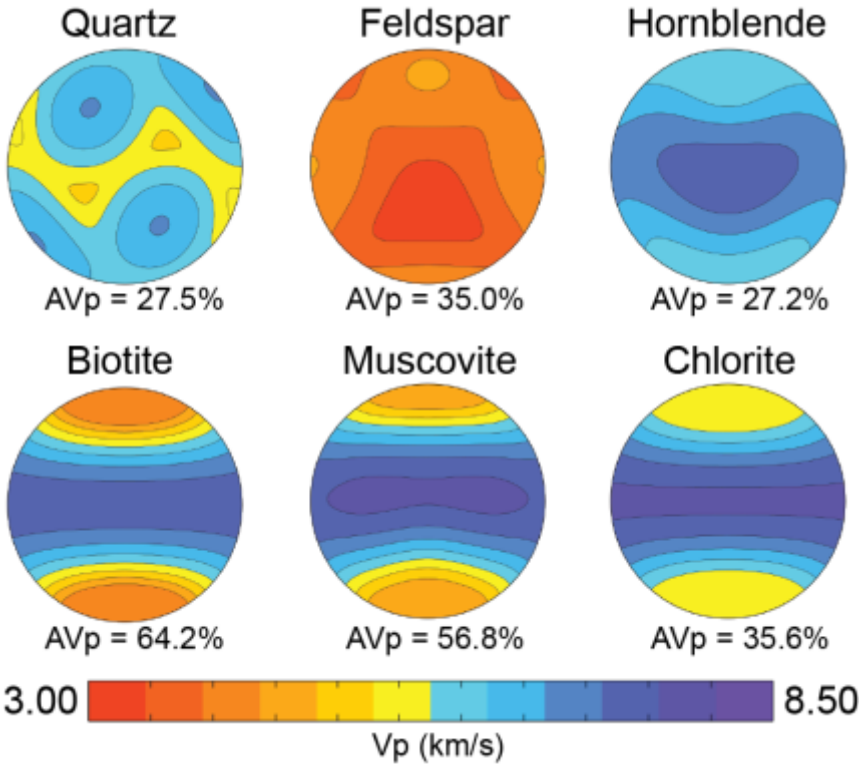

Figure 8. Vp velocity stereonets for single mineral tensors with Vp anisotropy listed below.

Quartz-rich rocks like CD06, CD24, and CD27 in particular, show the same Vp pattern as the quartz tensor. With the exception of CD27, the anisotropy is lowest for samples displaying this pattern. Almost all of the mafic samples have the same orthorhombic appearance as the hornblende single crystal (Figure 8). A study by Ji et al. (2013) shows similar patterns of amphibole in mafic gneiss. No distinct patterns for feldspar can be seen in Figures 3a and 3b but the more feldspar in a sample, the more likely that the sample would have the lowest anisotropy, and the lowest-order symmetry for that rock group.

4.3.2 Vp/Vs Patterns

The Vp/Vs stereonets in Figure 3a and b display some interesting patterns for some samples. These can also be related back to Vp/Vs patterns for individual mineral tensors (Figure 9). One patterns has a low Vp/Vs ring surrounding a high Vp/Vs perpendicular to the foliation (e.g. CD22 in 3a and CD05 in 3b). This pattern is typical of samples that contain large amounts of mica, particularly biotite, and is almost identical to the patterns for single crystal biotite, chlorite and muscovite (Figure 9).

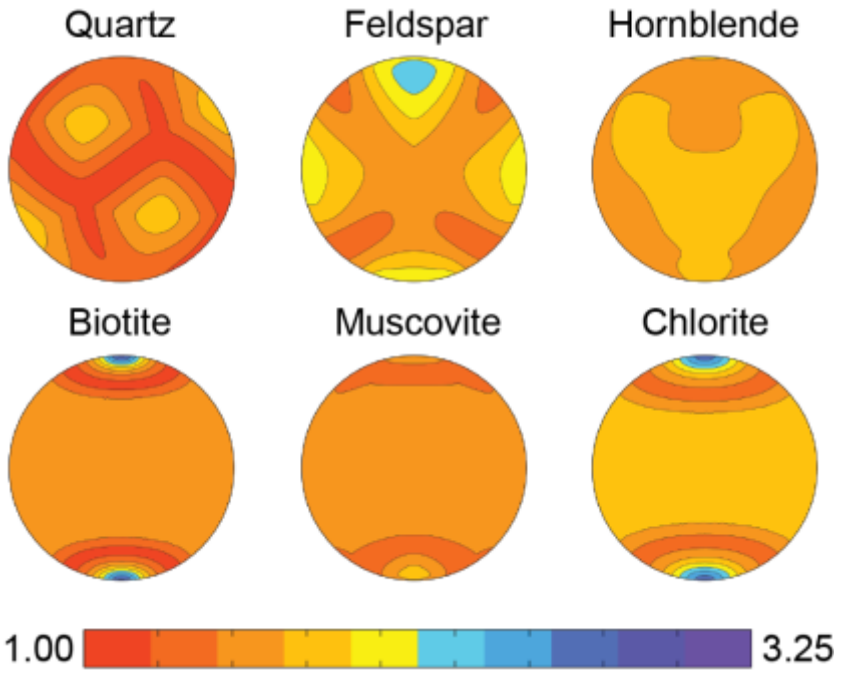

Figure 9. Vp/Vs stereonets for single mineral tensors

Another common pattern is a slight cross-girdle of low Vp/Vs perpendicular to the foliation. This pattern is evident in all of the felsic schist and some of the felsic gneiss samples. There are weaker cross-girdles in the mafic gneiss and the mafic schist. This pattern is found in samples that have significant amounts of feldspar (~>40%), and at least 10% mica. The remaining contributions from quartz and hornblende seem to lower the Vp/Vs ratio.

4.4 Implications for Seismic Modeling

This study has contributed to the development of a framework for interpreting lower crustal rock composition from seismic properties. The isotropic velocities and the anisotropies of each of the four rock types can be used to inform seismic models. Anisotropy is identified in receiver functions by azimuthal variations in amplitude and arrival time on both the radial and transverse components (Sherrington et al., 2004). An isotropic case with horizontal layering would only have arrival times on the radial component, and would have no azimuthal variation.

Dipping layers can exhibit similar patterns in the radial and transverse receiver functions as if anisotropy is present, so having accurate rock tensors as inputs into seismic models will help to distinguish between dipping layers and anisotropy. Also, for rocks rich in mica, the low and high Vp/Vs propagation directions are within 10 degrees of each other. Thus, if a schist layer is dipped even slightly, the apparent Vp/Vs will be dramatically different for the near-vertical propagation directions typical of receiver function studies. The Vp/Vs ratio can be used to determine the quartz content with some limitations depending on the type of crystal system as described by Erdman et al. (2013), so the potential effect of anisotropy on apparent Vp/Vs ratio is important to constrain.

Chapter 5: Conclusions

Samples with more quartz and feldspar, such as felsic gneiss, have lower seismic velocities and lower anisotropies. Felsic schist samples have higher anisotropies but not higher seismic velocities. Samples with hornblende, or the more mafic samples, have higher seismic velocities and higher anisotropies in the gneiss but lower anisotropies in the schist. Certain minerals seem to counteract each other in regards to anisotropy. Samples with equal amounts of quartz and amphibole vs mica will not be as anisotropic and will have higher orthorhombic components. Although mica seems to control anisotropy, varying combinations of quartz, feldspar, and amphibole can counteract the effect of mica.

To decrease uncertainty in seismic interpretations, and expand the seismic anisotropy database, future projects should also include the effects of total finite strain on anisotropy. Alternative ways of calculating the elastic tensor should also be explored. For example, the AEH calculation, which takes the compositional banding into account should be explored in addition to the volume averaging methods used in this study.

The results from this study contribute to the growing database of crustal elastic tensors. The relationships we report between particular mineral contents and anisotropic properties can be used to inform interpretations of seismic anisotropy. Our measured tensors, and mineralogic trends, can also be used as inputs in seismic inversions, which will improve the accuracy of these tensor inversions with respect to actual rock tensors, and decrease the required number of free parameters.

REFERENCES

Aleksandrov, K. S., and Ryzhova, T. V., 1961, The elastic properties of rock-forming minerals: II layered silicates: Izv. Acad. Sci. USSR Phys. Solid Earth, v. Engl. Transl., no. 11, p. 1165-1168.

Anderson, D. L., 1989, Theory of the Earth, Boston, Blackwell Scientific Publications, 366 p.:

Backus, G. E., 1965, Possible forms of seismic anisotropy of the uppermost mantle under oceans: Journal of Geophysical Research, v. 70, no. 14, p. 3429-3439.

Browaeys, J. T., and Chevrot, S., 2004, Decomposition of the elastic tensor and geophysical applications: Geophysical Journal International, v. 159, no. 2, p. 667-678.

Brownlee, S. J., Hacker, B. R., Salisbury, M., Seward, G., Little, T. A., Baldwin, S. L., and Abers, G. A., 2011, Predicted velocity and density structure of the exhuming Papua New Guinea ultrahigh-pressure terrane: Journal of Geophysical Research-Solid Earth, v. 116, p. 15.

Christen, N. I., and Crosson, R. S., 1968, Seismic anisotropy in upper mantle: Tectonophysics, v. 6, no. 2, p. 93-&.

Erdman, M. E., Hacker, B. R., Zandt, G., and Seward, G., 2013, Seismic anisotropy of the crust: electron-backscatter diffraction measurements from the Basin and Range: Geophysical Journal International, v. 195, no. 2, p. 1211-1229.

Hacker, B. R., and Christie, J. M., 1990, Brittle/ductile and plastic/cataclastic transitions in experimentally deformed and metamorphosed amphibolite: AGU Monograph, v. 56, p. 127-147.

Halchuk, S. C., and Mereu, R. F., 1990, A seismic investigation of the crust and Moho underlying the Peace River Arch, Canada: Tectonophysics, v. 185, no. 1-2, p. 1-19.

Hatcher, R. D., 2010, The Appalachian orogen: A brief summary: GSA Memoirs, v. 206, p. 1-19.

Ji, S. C., and Mainprice, D., 1988, Natural deformation dabrics of plagioclase - Implications for slip systems and seismic anisotropy: Tectonophysics, v. 147, no. 1-2, p. 145-163.

Ji, S. C., Shao, T. B., Michibayashi, K., Long, C. X., Wang, Q., Kondo, Y., Zhao, W. H., Wang, H. C., and Salisbury, M. H., 2013, A new calibration of seismic velocities, anisotropy, fabrics, and elastic moduli of amphibole-rich rocks: Journal of Geophysical Research-Solid Earth, v. 118, no. 9, p. 4699-4728.

Karabinos, P., 2002, Acadian extension around the Chester dome, Vermont: New England Intercollegiate Geologic Conference and New York State Geological Association Joint Meeting, p. C6-1-C6-20.

Klemperer, S. L., 1987, A relation between continental heat-flow and the seismic reflectivity of the lower crust: Journal of Geophysics-Zeitschrift Fur Geophysik, v. 61, no. 1, p. 1-11.

Kruhl, J. H., 1996, Prism- and basal-plane parallel subgrain boundaries in quartz: A microstructural geothermobarometer: Journal of Metamorphic Geology, v. 14, no. 5, p. 581-589.

Lee, J., Hacker, B., and Wang, Y., 2004, Evolution of North Himalayan gneiss domes: structural and metamorphic studies in Mabja Dome, southern Tibet: Journal of Structural Geology, v. 26, no. 12, p. 2297-2316.

Lloyd, G. E., Butler, R. W. H., Casey, M., Tatham, D. J., and Mainprice, D., 2011, Constraints on the seismic properties of the middle and lower continental crust: Geological Society, London, Special Publications, v. 360, no. 1, p. 7-32.

Mainprice, D., Bachmann, F., Hielscher, R., and Schaeben, H., 2015, Descriptive tools for the analysis of texture projects with large datasets using MTEX: strength, symmetry and components, *in* Faulkner, D. R., Mariani, E., and Mecklenburgh, J., eds., Rock

Deformation from Field, Experiments and Theory: A Volume in Honour of Ernie Rutter, Volume 409: Bath, Geological Soc Publishing House, p. 251-271.

Olsen, T. S., and Kohlstedt, D. L., 1984, Analysis of dislocations in some naturally deformed plagioclase feldspars: Physics and Chemistry of Minerals, v. 11, no. 4, p. 153-160.

Pavlenkova, N. I., 1992, The Kola Superdeep Drillhole and the nature of seismic boundaries: Terra Nova, v. 4, no. 1, p. 117-123.

Rosenfeld, J. L., 1968, Garnet rotations due to major Paleozoic deformations in southeast Vermont, *in* Zen, E., ed., Studies of Appalachian Geology, Northern and Maritime: New York, Wiley Interscience, p. 185-202.

Rudnick, R. L., and Fountain, D. M., 1995, Nature and composition of the continental crust: A lower crustal perspective: Reviews of Geophysics, v. 33, no. 3, p. 267-309.

Shao, T. B., Ji, S. C., Oya, S., Michibayashi, K., and Wang, Q., 2016, Mica-dominated seismic properties of mid-crust beneath west Yunnan (China) and geodynamic implications: Tectonophysics, v. 677, p. 324-338.

Sherrington, H. F., Zandt, G., and Frederiksen, A., 2004, Crustal fabric in the Tibetan Plateau based on waveform inversions for seismic anisotropy parameters: Journal of Geophysical Research-Solid Earth, v. 109, no. B2, p. 22.

Siegesmund, S., Kern, H., and Vollbrecht, A., 1991, The effect of oriented microcracks on seismic velocities in an ultramylonite: Tectonophysics, v. 186, no. 3, p. 241-251.

Siegesmund, S., and Kruhl, J. H., 1991, The effect of plagioclase textures on velocity anisotropy and shear-wave splitting at deeper crustal levels: Tectonophysics, v. 191, no. 1-2, p. 147-154.

Teyssier, C., and Whitney, D. L., 2002, Gneiss domes and orogeny: Geology, v. 30, p. 1139-1142.

Thompson, A. B. J., 1950, A gneiss dome in southeastern Vermont: PhD Thesis, Massachusetts Institute of Technology, p. 149.

Thompson, A. B. J., Robinson, P., Clifford, N. T., and Trask, N. J. J., 1968, Nappes and gneiss domes in west central New England, *in* Zen, E., ed., Studies of Appalachian Geology: New York, Wiley Interscience.

Ward, D., Mahan, K., and Schulte-Pelkum, V., 2012, Roles of quartz and mica in seismic anisotropy of mylonites: Geophysical Journal International, v. 190, no. 2, p. 1123-1134.

ABSTRACT

SEISMIC ANISOTROPY AS A FUNCTION OF MINERALOGY AND ROCK TYPE IN CHESTER GNEISS DOME, SOUTHEAST VERMONT

by

BRITTANY WATLING

May 2017

Advisor: Dr. Sarah Brownlee

Major: Geology

Degree: Master of Science

Our knowledge of composition and structure in middle and lower crustal rocks is limited due to restricted accessibility, and thus comes mainly from studies of seismic velocities. But isotropic seismic velocities are not sufficient to distinguish between the many possible rock types in the middle and lower crust. Seismic anisotropy is the directional dependence of seismic velocity, and may provide further constraints on mineralogy and rock type. This study is focused on characterizing the seismic anisotropy of rocks from the Chester dome in southeast Vermont. We have simplified the Chester dome rock types into four groups based on rock type and composition: gneisses (felsic (7) and mafic (4)), and schists (felsic (5) and mafic (5)). We calculated elastic tensors from electron backscatter diffraction (EBSD) measurements of mineral crystallographic preferred orientations. Results show that gneiss Vp anisotropy (AVp) ranges 4.0-14.8% and schist AVp ranges from 9.2-25.1%. On average, the mafic gneiss samples are slightly more anisotropic than the felsic gneiss but the felsic schist samples are more anisotropic than the mafic schist. Both mineralogy and rock type are important for controlling elastic properties, and thus seismic anisotropy has the potential for distinguishing between different rock types, and similar rock types with different mineralogy.

AUTOBIOGRAPHICAL STATEMENT

Brittany Watling has completed her Bachelor of Science in Environmental Geoscience from Michigan State University. She is now completing her Master of Science in Geology at Wayne State University.